

APPLIED SCIENCES AND ENGINEERING

Eyedrop-based macromolecular ophthalmic drug delivery for ocular fundus disease treatment

Jingjing Shen^{1†}, Huiqin Gao^{2,3†}, Linfu Chen¹, Yutong Jiang¹, Shu Li⁴, Yu Chao¹, Nanhui Liu¹, Yufei Wang¹, Ting Wei¹, Yan Liu^{2,3}, Jipeng Li^{2,3}, Muchao Chen¹, Jiafei Zhu¹, Juan Liang⁴, Xiaoyu Zhou⁴, Xiaofeng Zhang^{4*}, Ping Gu^{2,3*}, Qian Chen^{1*}, Zhuang Liu^{1*}

Therapeutic antibodies are extensively used to treat fundus diseases by intravitreal injection, as eyedrop formulation has been rather challenging due to the presence of ocular barriers. Here, an innovative penetrating carrier was developed for antibody delivery in eyedrop formulations. We found that fluorocarbon-modified chitosan (FCS) would self-assemble with proteins to form nanocomplexes, which could effectively pass across the complicated ocular structure to reach the posterior eye segments in both mice and rabbits. In a choroidal melanoma-bearing mouse model, eyedrops containing FCS/anti-PDL1 could induce stronger antitumor immune responses than those triggered by intravenous injection of anti-PDL1. Moreover, in choroidal neovascularization-bearing mouse and rabbit models, FCS/anti-VEGFA eyedrops effectively inhibited vascular proliferation, achieving comparable therapeutic responses to those observed with intravitreal injection of anti-VEGFA. Our work presents an effective delivery carrier to treat fundus diseases using eyedrop of therapeutic proteins, which may enable at-home treatment of many eye diseases with great patient compliance.

INTRODUCTION

The occurrence of chronic fundus oculi diseases such as diabetic retinopathy (1) and age-related macular degeneration (AMD) is continuously increasing due to the prolonged wearing of contact lenses (2), diabetes mellitus, and the increased elderly population. In recent years, many types of protein therapeutics, such as antibodies, are playing increasingly important roles in the treatment of eye diseases. Although noninvasive topical applications using eyedrops or ointments are the dominant dosage forms for the treatment of ocular surface diseases, efficient delivery of drugs, especially macromolecules such as antibodies, into the eyes is challenging due to complicated ocular structural barriers (3, 4). Systemic intravenous administration is the most commonly used route for therapeutic proteins. However, it would require overdosage if used for eye diseases to achieve effective local drug concentrations due to the presence of blood-eye barrier, and thus may induce various side effects. Therefore, systemic administration of antibodies for the treatment of fundus diseases has not been achieved in clinic. Intraocular injection (5) is able to directly deliver therapeutic proteins into the posterior segment of eyes with hypodermic needles, and it has become the standard treatment for fundus diseases. However, it still has the risk of endophthalmitis infection, bulbar bleeding, and retinal detachment (6–9). Therefore, there is a compelling need to develop efficient ocular drug delivery systems to shuttle macromolecules such as therapeutic proteins to the posterior segment of eyes.

To realize efficient delivery of ophthalmic drugs, various strategies have been developed. For instance, viscosity-enhancing polymers and in situ gelling systems (10) that are able to increase the retention time of drugs have been used to prepare different eyedrop formulations for extended ophthalmic drug delivery. However, both strategies are mostly suitable for ocular delivery of small molecular drugs and can hardly enhance the intraocular penetration of macromolecular therapeutics. A less invasive strategy using microneedles (11–13), which were originally developed for transdermal drug delivery, has been used to deliver drugs into the cornea and sclera. However, microneedles could still induce damages to eyes with risks of infections. Very recently, a polymeric nanomicelle system was reported to deliver macromolecular drugs for AMD treatment by prolonging their retention time on the eye. Although the therapeutic effect was demonstrated in mice with early choroidal neovascularization (CNV) using an extremely high dosage of antibodies (14), the mechanisms of corneal penetration of this polymeric micelle system, together with its pharmacokinetic and dynamic behavior in larger eyes, were still unclear. Hence, there is still a thorny and long way of exploration to go for noninvasive effective delivery of macromolecular ophthalmic drugs to treat fundus diseases.

To realize the noninvasive and effective delivery of macromolecular ophthalmic drugs into the fundus, we developed an innovative ocular barrier penetration carrier based on fluorocarbon-modified chitosan (FCS) for macromolecular ophthalmic drug delivery in eyedrop formulations (Fig. 1). Such FCS could self-assemble with therapeutic proteins such as antibodies via electrostatic interactions to form stable nanocomplexes, which showed effective ocular penetration ability by temporally opening the tight junctions in both cornea and conjunctiva tissue barriers. Using rat immunoglobulin G (IgG) as the model antibody, we demonstrated that the eyedrop formulation of FCS/IgG nanocomplexes with excellent ocular barrier penetration ability could effectively deliver IgG into the posterior segment of eyes (e.g., choroid and retina) in both mice and

Copyright © 2023 The Authors, some rights reserved; exclusive licensee American Association for the Advancement of Science. No claim to original U.S. Government Works. Distributed under a Creative Commons Attribution NonCommercial License 4.0 (CC BY-NC).

¹Institute of Functional Nano and Soft Materials (FUNSOM), Jiangsu Key Laboratory for Carbon-Based Functional Materials and Devices, Soochow University, Suzhou 215123, China. ²Department of Ophthalmology, Ninth People's Hospital, Shanghai JiaoTong University School of Medicine, Shanghai 200011, P. R. China. ³Shanghai Key Laboratory of Orbital Diseases and Ocular Oncology, Shanghai 200011, P. R. China. ⁴Department of Ophthalmology, Dushu Lake Hospital Affiliated to Soochow University, Suzhou, 215123 China.

†These authors contributed equally to this work.

*Corresponding author. Email: zliu@suda.edu.cn (Z.L.); chenqian@suda.edu.cn (Q.C.); guping2009@sjtu.edu.cn (P.G.); zhangxiaofeng@suda.edu.cn (X.Z.)

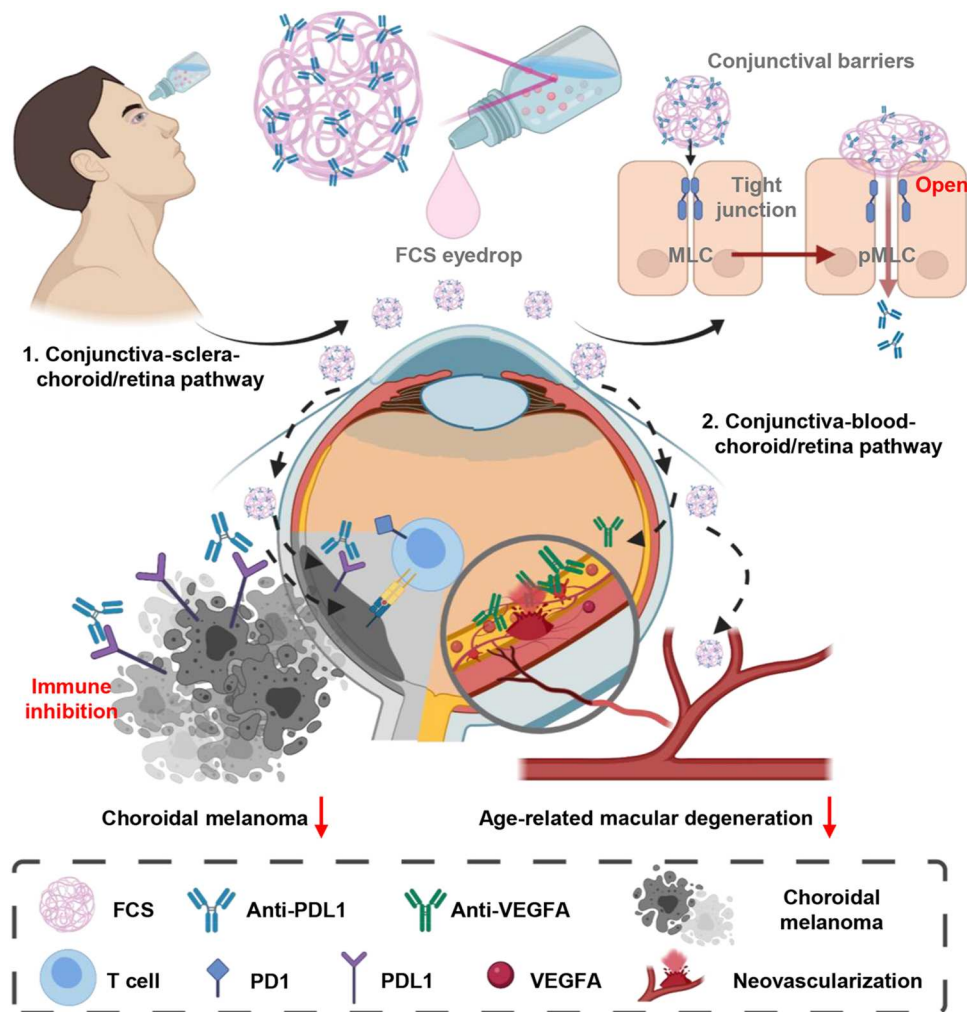


Fig. 1. Schematic illustration of FCS as the ocular barrier penetration carrier for effective macromolecular delivery for fundus disease treatment. FCS could induce the rearrangement of tight junction–associated proteins in corneal and conjunctival barriers and promote the penetration of macromolecules to reach the fundus. Successful treatments were achieved by FCS/anti-PDL1 nanocomplex eyedrops in a choroidal melanoma tumor model and FCS/anti-VEGFA nanocomplex eyedrops in AMD.

rabbits. Excitingly, we verified the excellent therapeutic outcomes in a choroidal melanoma-bearing mouse model with FCS/anti-programmed cell death ligand 1 (anti-PDL1) antibody (15) eyedrops, achieving improved antitumor responses compared to intravenously injected anti-PDL1. On the other hand, in CNV-bearing mouse model and rabbit models, we further demonstrated that FCS/anti-vascular endothelial growth factor–A antibody (anti-VEGFA or Eylea) (16) eyedrops resulted in comparable therapeutic effects to those realized with intraocular injection, although more overall antibody usage would be needed for the eyedrop formulation. Moreover, as systematically evaluated in both mice and rabbits, FCS exhibited negligible effects on the cornea, retina, and vision even for a long-term course. Therefore, eyedrop formulations based on the ocular barrier penetrating FCS would be paradigm-shifting for the convenient treatment of various eye diseases.

RESULTS

Preparation and screening of FCS/IgG nanocomplexes

FCS was obtained by grafting chitosan (CS) with perfluoroalkyl carboxylic acid (PFCA) via amide coupling (Fig. 2A). We synthesized a series of FCSs with different feeding ratios between CS and PFCA from 100:0 to 100:35. The fluorine element test was used to assess the degree of fluorocarbon substitution of FCS obtained at each feeding ratio (Fig. 2B). We then investigated the size distribution after mixing different FCSs with rat IgG at a weight ratio of 1:1. From the results of dynamic light scattering (DLS), we found that all the positively charged FCSs with different degrees of fluorocarbon substitution could form nanocomplexes with the negatively charged IgG. The nanocomplexes formed by mixing with IgG with FCS at a fluorocarbon substitution of 4.9% exhibited the most uniform sizes of approximately 200 nm (Fig. 2C). What is more, FCS/IgG was stored at 4°C with uniform and stable size for 5 weeks (fig. S1), which meant that the FCS/protein nanocomplex has great stability as eyedrops stored at 4°C.

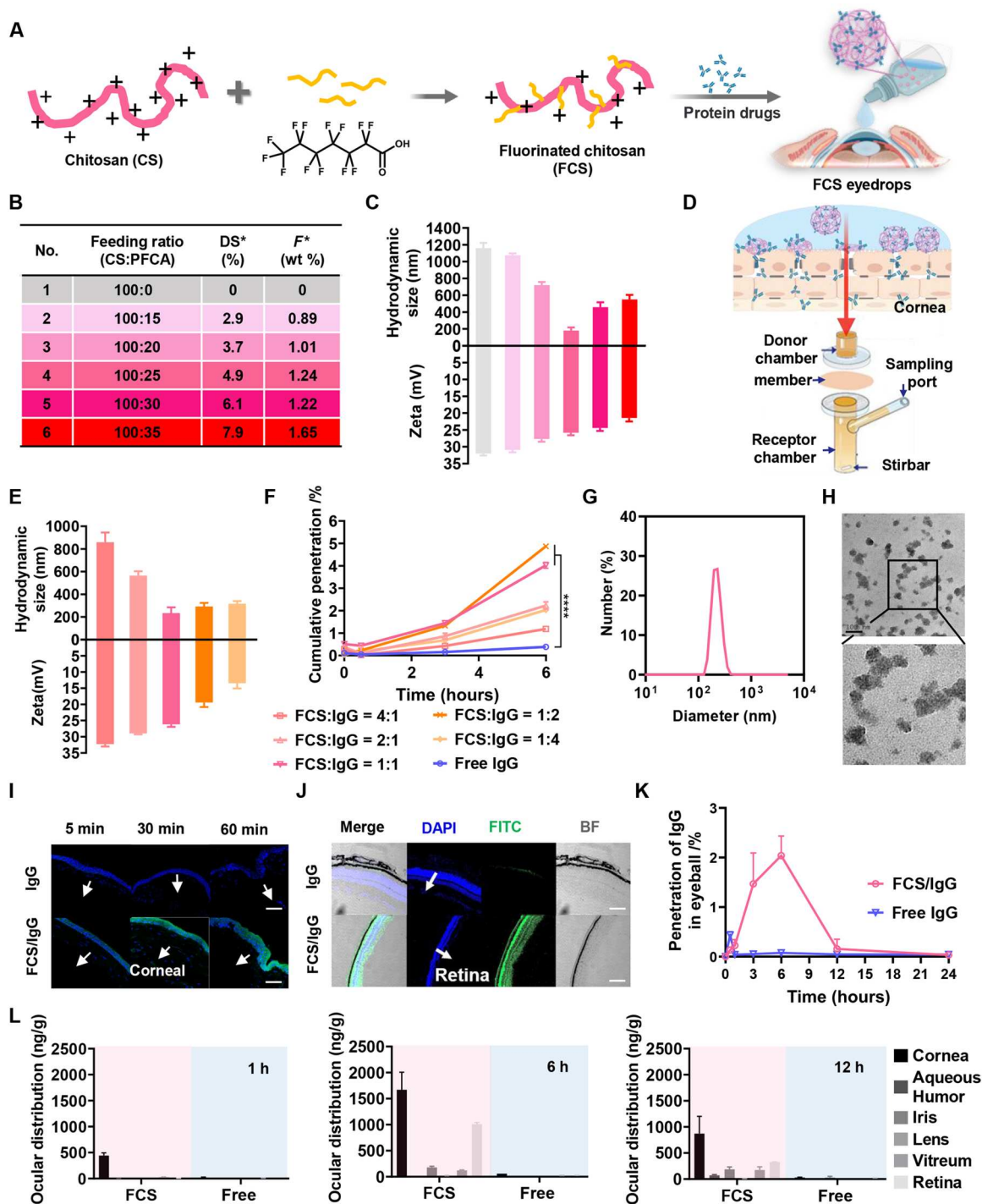


Fig. 2. Characterization of FCS/IgG nanocomplexes. (A) Illustration of the synthesis of FCS/IgG nanocomplexes. (B) FCS with different degrees of fluorination substitution. (C) Zeta potential and size distribution of FCS/IgG with different degrees of substitution. (D) Illustration of Franz transdermal diffusion cells with the rabbit cornea as the membrane. (E) Zeta potential and size distribution of FCS/IgG with different ratios of FCS and IgG. (F) Cumulative penetration percentages of different groups. (G) Size distribution of FCS/IgG with the ratio of FCS and IgG at 1:1. (H) TEM imaging of FCS/IgG with the FCS:IgG ratio at 1:1 (scale bar, 200 nm). (I) Confocal images of mouse corneas after applying the FCS/IgG-FITC nanocomplex at different time points; IgG-FITC (green) and 4',6'-diamidino-2-phenylindole (DAPI; blue) (scale bars, 200 μ m). (J) Confocal images of the mouse retina 6 hours after applying FCS/IgG-FITC nanocomplexes; IgG-FITC (green) and DAPI (blue) (scale bar, 200 μ m). (K) Penetration of rat IgG in the whole mouse eyeball after applying FCS/IgG or free IgG eyedrops. (L) Distribution of rat IgG in the cornea, aqueous humor, iris, lens, vitreum, and retina of rabbit eyes after applying different eyedrops for 1, 6, and 12 hours. Data were represented as means \pm SD. *P* values in (F) were calculated by using one-way ANOVA (**P* < 0.05 and *****P* < 0.0001).

Next, we used the Franz diffusion cell (17) with isolated rabbit corneas as a standardized method to evaluate the penetration abilities of FCS with different degrees of fluorocarbon substitutions against the cornea. In this experiment, different FCS/IgG nanocomplexes with IgG labeled by fluorescein isothiocyanate (FITC) were added into the donor chamber, and the transmitted IgG in the receptor chamber was measured according to the fluorescence signals at different time points (Fig. 2D and fig. S2). As shown in fig. S2, all nanocomplexes showed increased penetration ability across the cornea. Notably, FCS with a 4.9% fluorocarbon substitution degree showed the highest cornea penetration in the Franz diffusion cell and thus was chosen in the following experiments.

Using the optimized FCS, we further characterized FCS/IgG nanocomplexes formed using different proportions of FCS and IgG. From the DLS results, we found that the sizes of FCS/IgG nanocomplexes decreased and then increased as the IgG proportion increased (Fig. 2E). At an FCS:IgG weight ratio of 1:1, the formed nanocomplexes showed the smallest size with a uniform size distribution. Then, a corneal cumulative penetration experiment was further carried out to optimize the proportion of FCS and IgG. As shown in Fig. 2F, the cumulative penetration rates of FCS/IgG-FITC nanocomplexes with FCS:IgG ratios of 1:1 and 1:2 were 4.02 and 4.87%, respectively, which were significantly higher than those of the other groups. Notably, adding too much FCS to FCS/IgG nanocomplexes (with an FCS:IgG ratio at or above 2:1) would lead to the aggregation of those nanoparticles and thus reduced permeability efficiency. Considering the particle size and corneal cumulative penetration ability, we screened FCS/IgG with the optimal ratio at 1:1 for further experiments. As illustrated by transmission electron microscopy (TEM) imaging (Fig. 2, G and H), FCS/IgG prepared at this optimized ratio exhibited highly dispersed uniform spherical morphology with an average diameter of approximately 200 nm.

Topical ocular delivery with FCS/IgG nanocomplexes

To evaluate the *in vivo* ocular barrier penetration capability of FCS/IgG nanocomplexes, we detected the distribution of IgG-FITC in the cornea, retina, and whole eyeball of mice at different time points after treatment with FCS/IgG-FITC eyedrops (Fig. 2, I and J, and fig. S3). From the longitudinal section of mouse eyes, we found that at 1 hour after applying the eyedrop, notable fluorescent signals from IgG-FITC were observed from corneal epithelium to corneal endodermis in eyes of mice treated with FCS/IgG-FITC, while rather weak fluorescence signals were detected in the cornea of mice treated with free IgG-FITC (Fig. 2I). Strong fluorescence signals from IgG-FITC were observed in both the retina and choroid of mice 6 hours later in the FCS/IgG-FITC-treated group, indicating that FCS/IgG-FITC nanocomplexes could efficiently deliver antibodies into the fundus (Fig. 2J and fig. S4). Then, we measured the concentrations of IgG in the entire eyeballs at different time points by enzyme-linked immunosorbent assay (ELISA) after applying eyedrops of FCS/IgG or free IgG to calculate the penetration ratios. Excitingly, FCS/IgG nanocomplexes showed a high penetration efficiency of approximately 2.04% (Fig. 2K). Moreover, we further used ^{125}I -labeled rat IgG to measure the content of IgG in the interior of eyes with or without the help of FCS. As shown in fig. S5, FCS/ ^{125}I -IgG nanocomplexes showed the penetration efficiency of about 1.17 and 2.26% at 3 and 6 hours after eyedropping, respectively, consistent to the ELISA

results. It has been reported that about 90% of liquid eyedrops would flow out through the canthus and nasolacrimal duct (10). Thus, our observed protein penetration efficiency should set a record for the eyedrop delivery of therapeutic proteins as large as IgG (150 kDa).

Considering that the sizes of human eyes would be much larger than mouse eyes, we then investigated the ocular delivery efficiency of FCS/IgG nanocomplexes in the eyes of rabbits, whose eyes are on the semblable size scale of human eyes and have a more complete eye barrier system. The rabbits treated with free IgG-FITC or FCS/IgG-FITC eyedrops were euthanized at different time points, and their eyeballs were dissected and weighed after irrigation to detect the concentrations of IgG in different parts of the eye. FCS/IgG nanocomplexes mainly accumulated in the cornea in the first hour, and then the concentrations of IgG inside the eyes, especially in the retina and choroid, gradually increased over time (Fig. 2L). Meanwhile, the entire eyeball was collected for frozen sectioning. As seen in fig. S6, the fluorescence signals from IgG-FITC were gradually transformed from the cornea to retina and choroid over time, while there was nearly no fluorescence signal observed in the eyeball of rabbits treated with free IgG-FITC. Thus, FCS/IgG nanocomplexes also showed superior ocular barrier penetration ability in the eyes of rabbits.

Mechanistic studies of enhanced ocular delivery with FCS/IgG nanocomplexes

Encouraged by the superior ocular barrier penetration ability achieved by FCS/IgG nanocomplexes in the eyes of both mice and rabbits, we then tried to explore the mechanism of such ocular delivery. According to previous literature, CS has been demonstrated to disrupt the tight junctions (18–20) between cells to increase bypass delivery. Thus, to clarify whether FCS also has the ability to cross the cellular bypass pathway, we studied the expression and distribution of partial tight junction-associated proteins such as E-cadherin (21), occludin, and Zonula occludens protein-1 (ZO-1) (22) between human corneal epithelial cells (HCECs) (23). In this experiment, HCECs were incubated to form a compact monolayer with tight junction-related proteins closely arranged to mimic the corneal epithelial barrier. Then, the HCEC monolayer was incubated with FCS or CS (concentration, 100 $\mu\text{g}/\text{ml}$) for 12 hours, and the distribution and expression level of tight junction proteins between HCEC monolayers were further characterized by immunofluorescence staining and Western blotting, respectively. Both FCS and CS obviously caused the redistribution of tight junction-associated proteins, especially E-cadherin and occludin (Fig. 3A and fig. S7). Meanwhile, Western blotting revealed that the levels of tight junction-associated proteins in cells treated with FCS were nearly unchanged, while their levels in CS-treated cells were notably reduced (Fig. 3, B and D, and fig. S8). Our results indicated that CS could irreparably damage the epithelial barrier system, while FCS would only trigger redistribution of tight junction-associated proteins without affecting their overall expression levels.

Next, the classical cellular resistance test by measuring transepithelial electrical resistance (TEER) (24) was carried out to evaluate the opening of tight junctions of HCEC monolayers in the Transwell chamber. In this experiment, HCECs were cultured in the Transwell chamber, and their TEER was measured every 2 days until the TEER value remained unchanged, indicating the

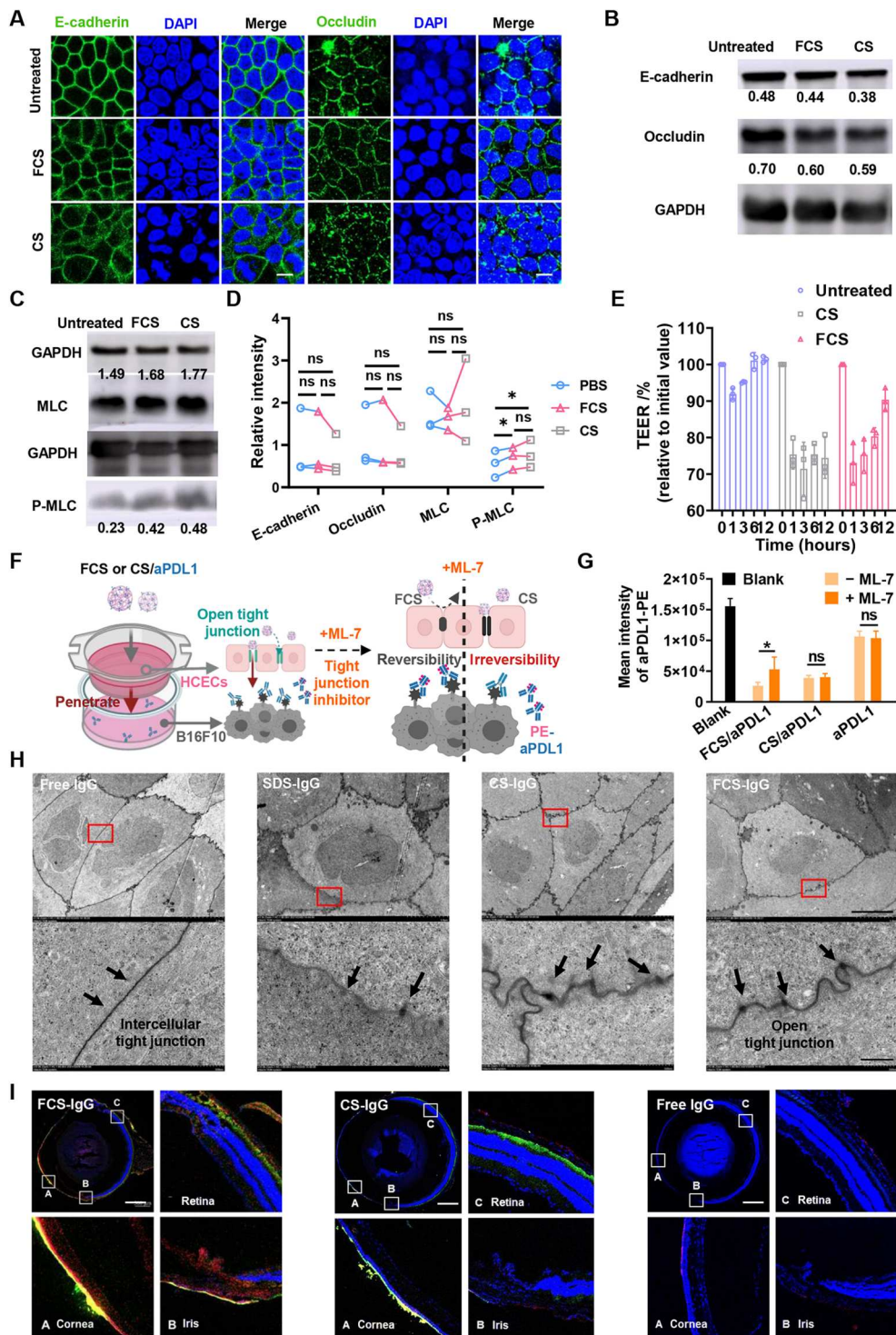


Fig. 3. Mechanisms of enhanced ophthalmic delivery of FCS/IgG nanocomplexes. (A) Immunofluorescence imaging indicating the distribution of tight junction-related proteins, including occludin and E-cadherin, after different treatments (scale bars, 10 μ m). (B to D) Western blotting images showing the expression of occludin, E-cadherin, MLC, and p-MLC and statistical analysis of MLCs and p-MLC in HCEC monolayers after incubation with different nanocomplexes. ns, not significant. (E) TEER of HCECs after different treatments for 1 hour. (F) Schematic showing the in vitro simulated corneal epithelial barrier consisting of an HCEC monolayer in the upper chamber and PDL1-expressing B16F10 cells in the lower chamber of a Transwell. (G) Intensity of fluorescence-labeled aPDL1 that combined with the remaining unblocked PDL1 antigen expressed in B16F10 cells. (H) TEM images of rabbit corneal epithelial tissue after treatment with PBS, SDS, FCS, or CS (scale bars, 5 μ m) and magnified TEM images (scale bar, 500 nm). (I) Confocal images of mouse eyeballs 6 hours after FCS-FITC/IgG-Cy5.5, CS-FITC/IgG-Cy5.5, or free IgG-Cy5.5 eyedrops were applied. The cornea, iris, and retina were partially magnified (scale bars, 500 μ m). Data were represented as means \pm SD. *P* values in (D) and (G) were calculated by using *t* test (**P* < 0.05).

successful establishment of an intact HCEC monolayer, which could be used to simulate the corneal epithelium *in vitro* (fig. S9). The intact HCEC monolayer was incubated with FCS or CS for 1 hour (concentration, 100 $\mu\text{g}/\text{ml}$), and then FCS and CS were removed. The value of TEER decreased by 27% 1 hour after adding FCS and returned to the normal level after incubation in fresh medium (with FCS removed) 12 hours later (Fig. 3E). In contrast, the TEER value of the HCEC monolayer incubated with CS could not recover even after incubation in fresh medium for 12 hours. To test whether long-time incubation with FCS or CS would affect the tight junctions between cells, we repeated the experiment and increased the incubation time with FCS or CS for up to 6 hours. As shown in fig. S10, the TEER of HCEC monolayer incubated with FCS and CS decreased to 45%, but only the TEER of HCEC monolayer in the FCS group returned to the normal level after incubation in fresh medium for 72 hours (with FCS removed). Thus, FCS could temporally promote transscleral delivery without causing permanent destruction of the ocular structural barriers.

Considering that the cytoskeletal structure is closely associated with the level of phosphorylation of myosin light chain 2 (pMLC) (25, 26), we further investigated the contents of MLCs and pMLCs in HCEC monolayers after FCS or CS treatment by Western blotting. As depicted in Fig. 3 (C and D), the phosphorylation level was up-regulated after FCS and CS treatment, indicating that both FCS and CS could regulate the phosphorylation of MLC to redistribute partial tight junction-associated proteins. Next, we used a Transwell chamber to study the ocular penetration ability of antibody, with a monolayer of HCECs to mimic the corneal epithelial barrier, and B16F10 mouse melanoma cells in the lower chamber of the Transwell. Interferon- γ (IFN- γ) was introduced to trigger the up-regulation of PDL1 expression in B16F10 cells (Fig. 3F) (27). Then, FCS/anti-PDL1, CS/anti-PDL1, and free anti-PDL1 (anti-PDL1 concentration, 100 $\mu\text{g}/\text{ml}$) were added to the upper chamber of the Transwell for 6 hours. It was found that both anti-PDL1 in the FCS/anti-PDL1 and CS/anti-PDL1 formulations could successfully pass through the HCEC monolayer and bind with B16F10 cells in the lower chamber, while free anti-PDL1 showed little penetration. Then, the HCEC layer was reincubated with fresh medium for another 12 hours to restore cellular activity and further incubated with FCS/anti-PDL1, CS/anti-PDL1, and free anti-PDL1 in the presence of the myosin light chain kinase inhibitor ML-7 (135.8 ng/ml), which could inhibit the phosphorylation of myosin to inhibit the rearrangement process of tight junctions (28, 29). With ML-7 to inhibit the phosphorylation of myosin, penetrated anti-PDL1 in the FCS/anti-PDL1 formulation was obviously reduced, while that in the CS/anti-PDL1 formulation remained nearly unchanged (Fig. 3G). Paracellular pathway is mainly associated with the expression of tight junction and adherens junction proteins, together with cytoskeletal rearrangement (30). Thus, the reduced expression of TJ or AJ proteins, or changed cytoskeletal rearrangement may open the paracellular pathway (31). Considering the change of tight junction proteins, we hypothesized that CS reduced the expression of HCEC-associated tight junction proteins (occludin) and adhesion proteins (E-cadherin) and altered the phosphorylation of MLC, while FCS only altered the phosphorylation of actin MLC to change the cytoskeleton of HCECs. Therefore, inhibition of MLC phosphorylation may only partially shield the

opening of cellular bypasses induced by CS, different from the functions of FCS.

Next, we studied the *in vivo* effect of FCS on the tight junctions of the cornea and its capability for the intraocular delivery of proteins. TEM imaging was performed to observe the structure of tight junctions of rabbit corneal epithelial tissues after treatment with FCS, CS, SDS [positive control (29)], and phosphate-buffered saline (PBS) eyedrops. Six hours later, the rabbits were sacrificed, and their corneas were harvested immediately and fixed for TEM imaging. As shown in Fig. 3H, compared with the control group, narrow gaps, such as a door opening a crack, were observed in the tight junctions between corneal cells of rabbits treated with FCS, indicating that FCS had the ability to rearrange the distribution of tight junction-associated proteins between rabbit corneal epithelial cells, promising for the delivery of macromolecular ophthalmic drugs into the eye via cellular bypass pathways. Notably, although cracks between tight junctions were also observed in the CS-treated group, the tight junctions became lighter and blurred, somewhat similar to those treated with SDS, a surfactant that is able to destroy cell membrane proteins.

To further study the delivery route of FCS/IgG or CS/IgG nanocomplexes in the eye, FCS or CS labeled with FITC (green) and IgG labeled with Cy5.5 (red) were used to locate the specific pathway of carriers and macromolecule drugs during the delivery process (Fig. 3I). Excitingly, Cy5.5 signals from IgG delivered by FCS emerged both from the corneal epithelium to the corneal endodermis and from the conjunctive sclera and choroid to the retina. Considering the long distance of corneal approach to the fundus, we speculated that FCS/IgG might enter the eye through the conjunctiva-sclera-choroid-retina pathway. In view of the rich vasculature in subconjunctiva, FCS/IgG may migrate into periocular vascular microcirculation and then accumulate into the choroid and retina. We then measured the concentration of IgG in the blood of mice at different time points after FCS (or CS)/IgG eyedrop application. As shown in fig. S11, IgG could be detected in the blood of periocular vascular microcirculation, and the concentration of IgG in the FCS/IgG group was obviously higher than that in the CS/IgG group. Thus, both FCS/IgG and CS/IgG would be transported into the periocular blood vessels. Then, we tested the stability of FCS/IgG and CS/IgG in the serum environment. As shown in table S1, after 3-hour incubation in fetal bovine serum (FBS) (PBS containing 10% serum), FCS exhibited more stable binding ability to IgG, and only about 29.44% of the formed nanocomplexes were dissociated, while 61.52% of CS/IgG nanocomplexes were dissociated. Thus, more FCS/IgG would accumulate into the periocular vascular microcirculation and go through the conjunctiva-blood-choroid/retina pathway.

Safety assessment of FCS

Encouraged by the efficient ophthalmic delivery of macromolecules achieved by FCS, we then evaluated the biocompatibility of FCS as an eyedrop component in mice. First, healthy mice were divided into five groups and treated with different eyedrops, including PBS, FCS, CS, and SDS (concentration at 2 mg/ml, 5 μl every time) twice every day. Then, standard detection techniques including slit-lamp microscope, optical coherence tomography (OCT), and tonometry were used to measure the fluorescein cornea staining, corneal thickness, retinal thickness, and intraocular pressure (IOP) of mice on weeks 2 and 4, respectively. On the fourth week,

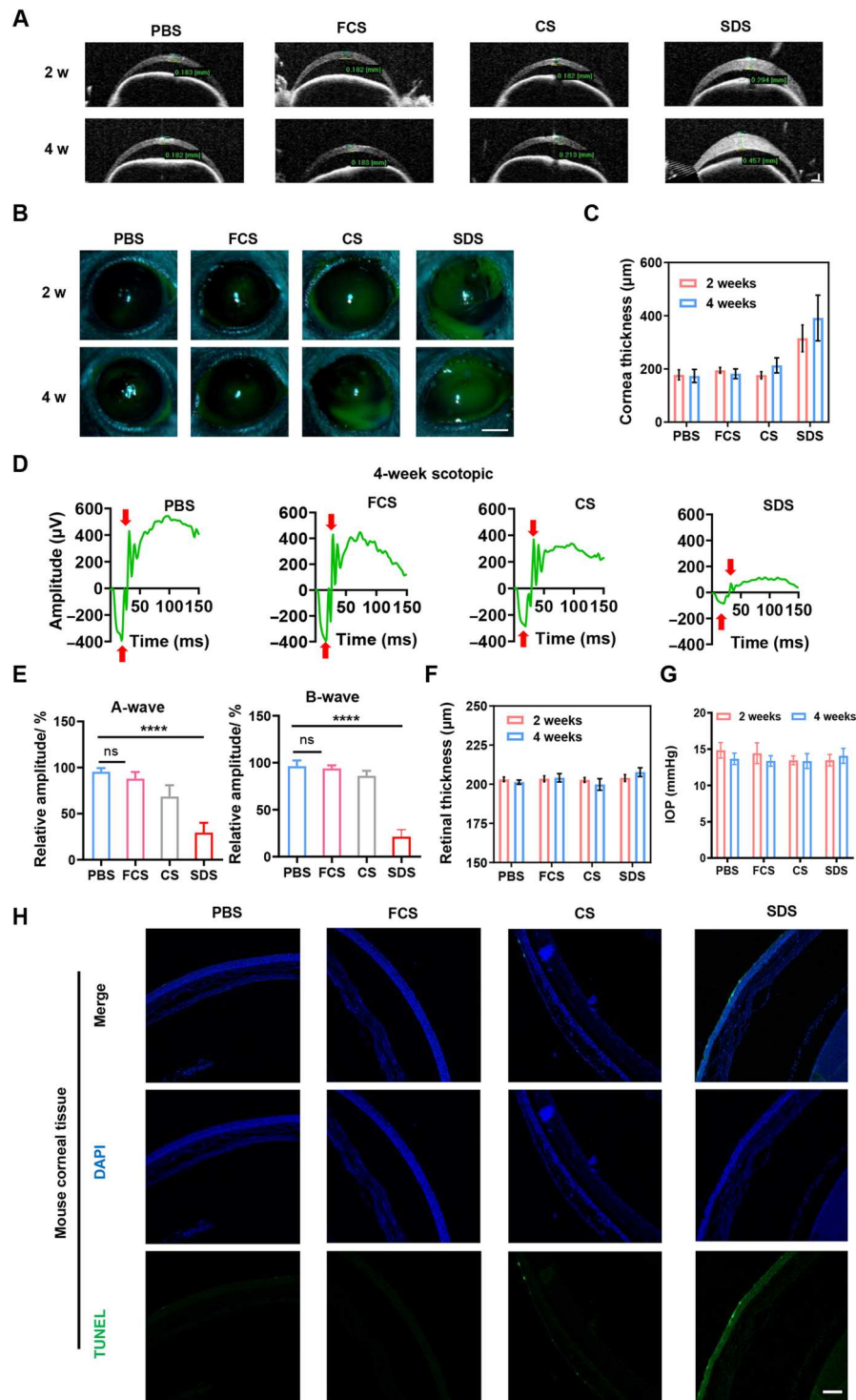


Fig. 4. Safety assessment of FCS. (A) Representative images of OCT of cornea treated with PBS, FCS, CS, or SDS eyedrops for 2 or 4 weeks (scale bar, 200 μm). (B) Representative images of fluorescein cornea staining of mouse eyes by slit-lamp microscopy treated with PBS, FCS, CS, or SDS eyedrops for 2 or 4 weeks (scale bar, 1 mm). (C) Statistical analysis of corneal thickness according to the OCT images. (D and E) Representative ERG waves of mouse eyes treated with PBS, FCS, CS, or SDS eyedrops for 4 weeks and statistical analysis of A waves and B waves. (F) Statistical analysis of retinal thickness treated with PBS, FCS, CS, or SDS eyedrops for 2 or 4 weeks. (G) Statistical analysis of IOPs of eyes in mice treated with PBS, SDS, CS, and FCS eyedrops on week 2 or week 4. (H) TUNEL staining of corneal tissues of mice treated with PBS, SDS, CS, and FCS eyedrops for 4 weeks (scale bar, 200 μm). Data were represented as means \pm SD. *P* values in (E) were calculated by using one-way ANOVA (*****P* < 0.0001).

the visual function of mice was evaluated by electroretinogram (ERG) under scotopic conditions. As shown in Fig. 4 (A and B), the corneas of mice treated with SDS showed turbidity with corneal defects and ulcers, while the corneas of mice treated with PBS, FCS, or CS showed nearly no abnormalities. We further calculated the corneal thickness according to the images of cornea by ImageJ (Fig. 4C). It was observed that the corneal thickness increased in SDS-treated groups, and the corneal and retinal thicknesses showed no apparent difference between mice in PBS-, FCS-, or CS-treated groups for 4 weeks. Moreover, according to the statistics of A waves and B waves in scotopic condition measured by ERG (Fig. 4, D and E), we found that FCS and CS exhibited nearly no effect on the retina of mice, indicating that FCS and CS exhibited negligible effect on the visual function of mice. However, mice treated with SDS showed an obvious decrease in both A and B waves under scotopic conditions, reflecting damage to both the inner and outer layers of the retina (Fig. 4F). In addition, compared to the control group, the IOP of all mice treated with FCS eyedrops was within the normal range, indicating that the long-term use of FCS did not cause an increase in IOP, avoiding side effects such as glaucoma (Fig. 4G). Last, terminal deoxynucleotidyl transferase-mediated deoxyuridine triphosphate nick end labeling (TUNEL) was performed to evaluate the necrotic effects induced on the corneas in different groups. As shown in Fig. 4H, while SDS induced serious damage to corneal tissues, FCS triggered negligible damage to corneal tissues.

Next, to evaluate the potential systemic toxicity of FCS, the major organs, including eye, heart, liver, spleen, lung, and kidney, from the above treated mice were collected for hematoxylin and eosin (H&E) staining (fig. S12). Blood samples of mice in different groups were also collected for hematological analysis (fig. S13). Both the histological H&E staining and hematological analysis results indicated that both CS and FCS induced nearly no systemic toxicity to mice after long-term administration. Moreover, the concentrations of transforming growth factor- β (TGF- β), tumor necrosis factor- α (TNF- α), interleukin-1 β (IL-1 β), IL-6, and IL-4 in eyes or blood samples analyzed by ELISA showed that long-term application of both CS and FCS caused negligible local ocular inflammatory storm (fig. S14).

Treatment of choroidal melanoma using FCS/anti-PDL1 eyedrops

Choroidal melanoma is one of the most common intraocular malignancies in adults and represents approximately 5% of all melanomas (32). Ophthalmectomy (33) and laser ablation (34) are common clinical therapeutic strategies for intraocular cancer. Although choroidal melanoma at an early stage can be successfully cured by ophthalmectomy, approximately 50% of patients with choroidal melanoma have liver metastasis and exhibit low survival rates (choroidal melanoma metastasis is shown in fig. S15). Notably, ophthalmectomy is not the preferred treatment for patients and usually causes serious psychological stress to patients without guaranteed survival. Cancer immunotherapy, especially immune checkpoint blockade (35, 36), has achieved excellent therapeutic results to treat different types of tumors. However, in view of the complex ocular barrier, systemic administration (37, 38) of immune checkpoint antibodies may be ineffective for intraocular cancer treatment. Considering the excellent ocular barrier penetration ability of antibodies achieved by FCS, we tried to explore the possibility

of using FCS/anti-PDL1 nanocomplex eyedrops for local noninvasive treatment of choroidal melanoma.

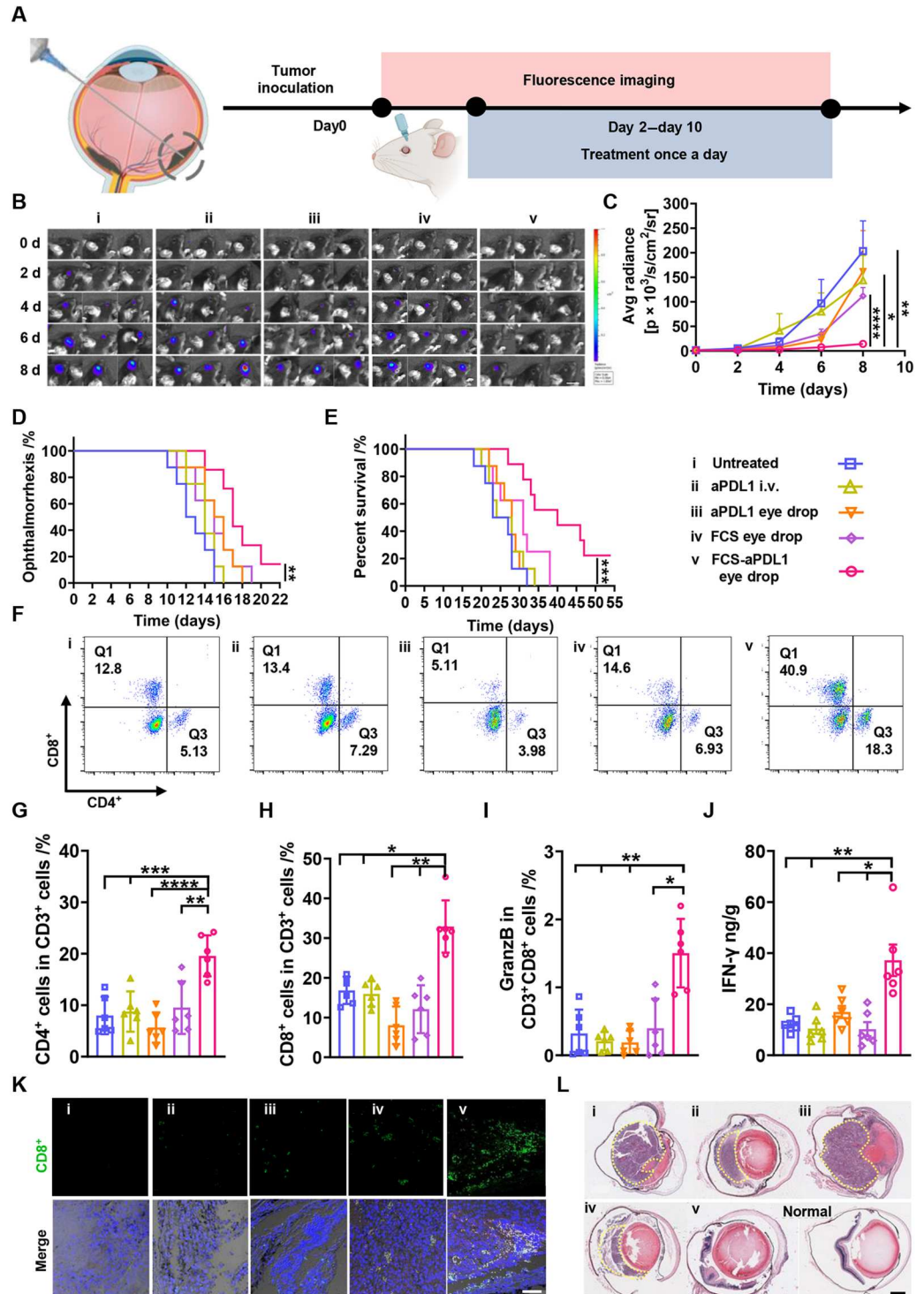
To demonstrate the ocular barrier penetrating ability of our FCS carrier for effective delivery of macromolecular ophthalmic drugs, we chose a simple ophthalmic tumor model by injecting Luc-B16F10 melanoma cells in subretinal space, as a proof of concept. Here, a murine choroidal melanoma tumor model was established by subretinal injection of Luc-B16F10 melanoma cells into the right eye of each mouse using a Hamilton microsyringe (39). Before the therapeutic experiment, we first studied the activity of anti-PDL1 after assembly with FCS by circular dichroism and ELISA. The original structure and binding affinity of anti-PDL1 remained nearly unchanged owing to the noncovalent interaction between FCS and antibodies (fig. S16). Then, C57BL/6 mice bearing choroidal melanoma were randomly divided into five groups for the following treatments: (i) PBS eyedrops (5 μ l/day \times 8 days), (ii) intravenous administration of anti-PDL1 (total dosage of anti-PDL1: 4 mg/kg, 1 mg/kg for each time), (iii) free anti-PDL1 eyedrops (total dosage of anti-PDL1: 4 mg/kg, 5 μ l/day \times 8 days), (iv) FCS eyedrops (total dosage of FCS: 4 mg/kg, 5 μ l/day \times 8 days), and (v) FCS/anti-PDL1 eyedrops (total dosage of anti-PDL1: 4 mg/kg, total dosage of FCS: 4 mg/kg, 5 μ l/day \times 8 days) (Fig. 5A).

The therapeutic results after different treatments were evaluated according to the bioluminescence signals from B16F10 choroidal melanoma cells imaged by the *in vivo* imaging system. As shown in Fig. 5 (B and C) and fig. S17, the eyes of mice treated with FCS/anti-PDL1 eyedrops exhibited relatively low bioluminescence signals, indicating the obviously delayed growth of choroidal melanoma in this group. In contrast, intravenous injection of free anti-PDL1 or eyedrops of free anti-PDL1 showed negligible therapeutic effects due to the existence of the blood-eye barrier and complex ocular structural barriers, respectively, both of which restricted the intraocular penetration of anti-PDL1. From the survival of mice after different treatments, we found that the mice treated with FCS/anti-PDL1 eyedrops showed obviously prolonged defined survival (according to the extent of mouse ophthalmorrhexis) and morbidity-free survival (Fig. 5, D and E). In the parallel experiment, mice were sacrificed on day 12, and their eyeballs containing choroidal melanoma were collected, photographed, and embedded in paraffin for H&E staining. From the images of eyeballs collected from mice in different groups, we could see that the volume of choroidal melanoma tumors in the FCS/anti-PDL1 eyedrop-treated group was the smallest and the eyeballs were the most integrated (fig. S18). Moreover, according to the H&E staining of eye slices, the eyes collected from FCS/anti-PDL1 eyedrop-treated mice showed the least amount of melanoma cancer cells compared to the other groups (Fig. 5I). Thus, FCS could overcome the eye barrier and successfully deliver anti-PDL1 into choroidal melanoma, effectively inhibiting the growth of cancer cells inside mouse eyes.

Inspired by the effective therapeutic results achieved by FCS/anti-PDL1 eyedrops, we then studied the immune responses by flow cytometry analysis and immunofluorescence staining of collected choroidal melanoma tumors. As shown in Fig. 5 (F and H) and fig. S19, the percentages of CD4⁺ and CD8⁺ cells were obviously increased in FCS/anti-PDL1 eyedrop-treated mice. Excitingly, the percentage of granzyme B-positive (GranzB⁺) CD8⁺ T cells also showed an obvious increase in mice after FCS/anti-PDL1 eyedrop treatment (Fig. 5I), indicating that the successfully delivered anti-

Fig. 5. FCS/anti-PDL1 eyedrops for choroidal melanoma treatment. (A) Schematic illustration of establishing choroidal melanoma and the design of animal experiments.

The experimental groups included (i) untreated, (ii) intravenous injection of anti-PDL1, (iii) anti-PDL1 eyedrops, (iv) FCS eyedrops, and (v) FCS/anti-PDL1 eyedrops. (B) Representative *in vivo* bioluminescence images of mice with Luc-B16F10 choroidal melanoma after different treatments (scale bar, 1 cm). (C) Average bioluminescence signal intensities from tumors after different treatments. (D) Cumulative ophthalmorrhexis-free survival of mice in different groups. (E) Cumulative modality-free survival rate of mice in different groups. (F) Representative fluorescence-activated cell sorting analysis of CD8⁺ and CD4⁺ T cells in eyes collected from mice after different treatments. (G to I) Percentages of CD4⁺ T cells, CD8⁺ T cells in CD3⁺ cells, and GranzB⁺ T cells in CD3⁺CD8⁺ cells analyzed by flow cytometry. (J) Concentration of IFN- γ in eyes after different treatments evaluated by ELISA. (K) Representative immunofluorescence images indicating the infiltration of CD8⁺ T cells around choroidal melanoma (scale bar, 50 μ m). (L) Representative H&E staining slices of mouse eyes with choroidal melanoma in different groups (scale bar, 500 μ m). Data were represented as means \pm SD. *P* values in (C) and (G) to (J) were calculated by using one-way ANOVA (**P* < 0.05, ***P* < 0.01, ****P* < 0.001, and *****P* < 0.0001). *P* values in (D) and (E) were calculated by using unpaired *t* test (**P* < 0.05, ***P* < 0.01, and ****P* < 0.001).



PDL1 into choroidal melanoma tumors could up-regulate the percentage of cytotoxic T lymphocytes to attack cancer cells. Moreover, according to the immunofluorescence staining and quantified analysis of choroidal melanoma tissues, we found that the number of CD8⁺ T cells was significantly increased in tumors of mice with FCS/anti-PDL1 eyedrop treatment, implying that this special eyedrop treatment would be a potent strategy to recruit CD8⁺ T

cells into choroidal melanoma tumors (Fig. 5, H and K). We further analyzed the related cytokines in treated tumors by ELISA. As expected, IFN- γ showed significant up-regulation in choroidal melanoma from mice treated with FCS/anti-PDL1 eyedrops (Fig. 5J). As a proof of concept, our results using a skin melanoma cell line (B16F10) to mimic the uveal melanoma model have demonstrated the effective immune activation after efficient

delivery of anti-PDL1 into choroidal tumors with the help of FCS. In future studies, however, it would be more clinically relevant to test our strategy with the tumor model created by uveal melanoma cells and use our FCS-based eyedrop formulation to deliver tebentafusp, a bispecific fusion protein demonstrated to be effective for clinical treatment of uveal melanoma (40, 41).

Alleviating CNV in mice using FCS/anti-VEGFA eyedrops

Neovascular AMD (NV-AMD), characterized by CNV, affects a wide range of people worldwide. The VEGF family member VEGFA (also named VEGF) and its receptor VEGFR2 contribute to the pathogenesis of CNV (42). Repeated intravitreal injection of anti-VEGF is the gold standard method for NV-AMD treatment in the clinic but suffers from rather low patient compliance and serious side effects. Thus, noninvasive ophthalmic delivery of anti-VEGF may provide a new possibility for NV-AMD treatment. Here, FCS/anti-VEGFA nanoparticles were prepared via self-assembly for the treatment of NV-AMD (Fig. 6A). We first used laser photocoagulation to induce CNV in the eyes of mice according to the standard protocol (43) to establish the experimental wet-AMD model. First, by using fundus fluorescein angiography (FFA) to measure the hyperfluorescence of sodium fluorescein in the CNV lesions, we observed the generation of new but fragile blood vessels branching through the Bruch membrane to the choroid and retina from the preexisting vessels, which would cause pathological vascular leakage due to increased microvascular permeability (fig. S20). In addition, OCT and H&E staining assays revealed an obvious increase in CNV lesion thickness, further demonstrating the successful establishment of the experimental wet-AMD model 7 days after laser photocoagulation. Then, the CNV-bearing mice were randomly divided into five groups: (i) PBS eyedrops (5 μ l/day \times 14 days), (ii) anti-VEGFA eyedrops (anti-VEGFA: 2 mg/ml \times 5 μ l \times 14 days), (iii) FCS eyedrops (FCS: 2 mg/ml \times 5 μ l \times 14 days), (iv) FCS/anti-VEGFA eyedrops (anti-VEGFA: 2 mg/ml \times 5 μ l \times 14 days, anti-VEGFA:FCS = 1:1), and (v) intravitreal injection of anti-VEGFA (anti-VEGFA: 10 mg/ml \times 5 μ l, one-time injection).

Next, we observed the retinas of CNV-bearing mice by FFA and OCT 2 weeks after different treatments. As shown in Fig. 6 (B and D), the symptoms of CNV in mice after being treated with FCS/anti-VEGFA eyedrops were obviously reduced, reaching a level close to that of mice with intravitreal injection of anti-VEGFA. We then carried out statistical analysis of the fluorescence intensities of fluorescein sodium in the leaked blood vessels (figs. S21 and S22), as well as the area and thickness of CNV lesions (Fig. 6, C and E) by ImageJ. Excitingly, both the relative fluorescence intensities of fluorescein sodium and the area and thickness of CNV lesions were obviously decreased after treatment with FCS/anti-VEGFA eyedrops or intravitreal injection of anti-VEGFA. However, in the other control groups, nearly no therapeutic results were observed. Then, ERG was used to evaluate the functional changes of photoreceptors of mice after different treatments. As shown in Fig. 6F, compared to the CNV-bearing mice in other groups, the CNV-bearing mice treated with FCS/anti-VEGF eyedrops or intravitreal injection of anti-VEGF showed significantly improved scotopic responses. From the statistical analysis, A waves and B waves in the scotopic condition in both the intravitreal injection and FCS/anti-VEGF eyedrop-treated groups were obviously increased (Fig. 6G and fig. S23). In addition, the B waves in the photopic condition in the

groups of intravitreal injection and FCS/anti-VEGF eyedrop-treated were also increased (fig. S24). At the end of treatment, the eyes were collected for pathological analysis. As shown in fig. S25, compared with the control and free antibody groups, the FCS/anti-VEGFA-treated eyes showed remission of CNV symptoms, including no further expansion of Bruch's membrane damage and notably reduced tissue proliferation. In contrast, mice in other groups still showed severe retinal vascularization, leading to severe dysfunction of both inner and outer retinal layers. Thus, noninvasive fundus delivery of anti-VEGFA in the formulation of FCS/anti-VEGFA demonstrated excellent therapeutic results in a preclinical mouse model of CNV, achieving comparable effects to those observed with intravitreal injection of anti-VEGFA in CNV mice.

AMD has been widely reported to be associated with inflammation (44, 45). Thus, we evaluated inflammation in the retina by detecting IL-1 β (46), one of the important cytokines associated with inflammatory diseases. As shown in the immunofluorescence staining images, compared to the CNV-bearing mice with other treatments, both FCS/anti-VEGFA eyedrops and intravitreal injection of anti-VEGFA could significantly reduce the level of IL-1 β . In addition to IL-1 β , we also measured the expression of VEGF, a representative marker of CNV progression and deterioration, and RPE65, a key component of the visual cycle closely related to the regeneration of visual pigments. It was found that the expression of VEGF in the retina of mice with intravitreal injection of anti-VEGF or dropping FCS/anti-VEGF showed a significant decrease. More excitingly, the CNV mice after either intravitreal injection of anti-VEGFA or dropping of FCS/anti-VEGFA exhibited obviously increased expression of RPE65 (fig. S26). Together, with the help of FCS, effective intraocular delivery of anti-VEGFA was achieved, which was able to decrease the expression of VEGF, promote the regeneration of retinal pigment cells, and reduce CNV-related inflammation, such as the expression of IL-1 β , successfully alleviating CNV in mice. The above results demonstrated that FCS could successfully deliver anti-VEGFA into the choroid and retina of the mice eye to inhibit angiogenesis, reaching the therapeutic responses comparable to that achieved by intravitreal injection of anti-VEGFA.

Alleviating CNV in rabbits using FCS/Eylea eyedrops

To verify the therapeutic efficiency achieved by noninvasive ophthalmic delivery in larger eyes with more complex structures, we established a CNV model in purple blue rabbits using laser photocoagulation following a reported protocol (47, 48). Because of the presence of uvea and Bruch's membrane in the eyes of purple blue rabbits, we attempted to establish a rabbit CNV model using laser photocoagulation to damage Bruch's membrane (48). Note that only purple blue rabbits (colored rabbits), but not conventionally used New Zealand rabbits (white rabbits), have pigments on their choroid and thus are suitable for building such a CNV model. For each rabbit, we performed laser photocoagulation at nine laser burns near the inferior lumen of the optic nerve head. The symptoms of CNV in rabbits were monitored 3 and 6 days after laser photocoagulation. Much more serious fluorescein sodium leakage was observed in the neovascularization around the laser spots 6 days later, signifying that the CNV model in purple blue rabbits was successfully established (fig. S27).

Then, the CNV-bearing rabbits were randomly divided into three groups: (i) PBS eyedrops (25 μ l/day \times 21 days, $n = 10$), (ii) FCS/Eylea nanocomplex eyedrops (Eylea: 1.4 mg per eye, 2 mg/ml

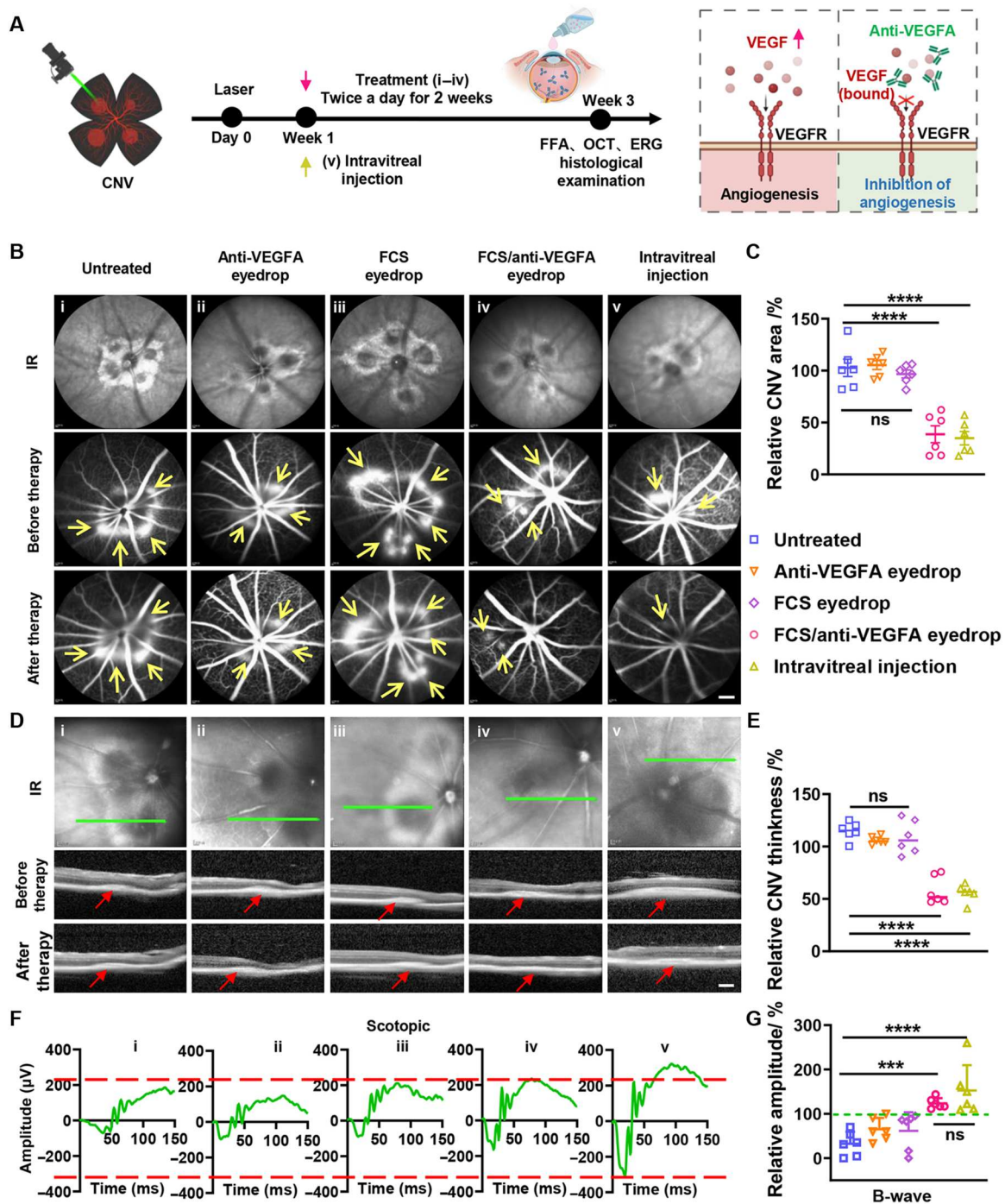


Fig. 6. FCS/anti-VEGFA eyedrops for CNV treatment in mice. (A) Schematic illustration of the establishment of NV-AMD and the design of animal experiments. The experimental groups included (i) untreated, (ii) intravitreal injection of anti-VEGFA, (iii) anti-VEGFA eyedrops, (iv) FCS eyedrops, and (v) FCS/anti-VEGFA eyedrops. (B) Representative FFA images of individual lesions in CNV-bearing mice before and after different treatments. The arrows point to CNV positions (scale bar, 10 µm). (C) Statistical analysis of relative areas of leakage of angiogenic vessels in CNV mice by ImageJ. (D) Representative OCT images of individual lesions in CNV-bearing mice before and after different treatments. The arrows point to CNV positions (scale bar, 200 µm). (E) Statistical analysis of the thickness of CNV in (D) by ImageJ. (F) Representative ERG wave responses of CNV-bearing mice after different treatments under scotopic conditions. The dashed line indicates the A and B wave values of the positive control group. (G) Statistical analysis of B waves measured by ERG after different treatments under scotopic conditions. Data were represented as means ± SD. *P* values in (C), (E), and (G) were calculated by using one-way ANOVA (****P* < 0.001 and *****P* < 0.0001).

for 25 μ l twice a day for the first 7 days and then 25 μ l/day for the next 14 days, $n = 10$), and (iii) intravitreal injection of Eylea (Eylea: 0.5 mg per eye, 10 mg/ml for 50 μ l one-time injection, $n = 8$) (Fig. 7A and fig. S28). During the treatment, FFA examination was carried out in rabbits on day 0 (pretreatment), day 7, and day 21 to monitor the changes in CNV. According to the standard clinical grading of CNV, each rabbit eye was professionally scored by three ophthalmologists in a double-blind manner. Compared to the nonintervention group (average score 0 day = 2.79; average score 21 day = 3.20), both intravitreal injection of Eylea (average score 0 day = 2.74; average score 21 day = 1.91) and osmotic FCS/Eylea eyedrops (average score 0 day = 2.68; average score 21 day = 2.22) relieved CNV in purple blue rabbits (Fig. 7, B and C). According to the quantified leakage signals of fluorescein sodium in laser spots by ImageJ (Fig. 7D), the fluorescence signals were reduced on days 7 and 21 with the treatment of either FCS/Eylea eyedrops or intravitreal injection of Eylea. As shown in the H&E staining images (Fig. 7E), obvious proliferation of blood vessels and tissues to the choroid and retina was observed with laser photocoagulation, and the area of proliferative tissues was significantly reduced after 1 month of treatment with FCS/Eylea eyedrops or intravitreal injection. In addition, the expression of VEGF and neovascularization were also obviously reduced with FCS/Eylea eyedrops or intravitreal injection of Eylea, as exhibited in the immunofluorescence staining eye section (Fig. 7F). The above results demonstrated that FCS could successfully deliver therapeutic antibody such as Eylea to the posterior segment of the rabbit eye (choroid and retina) to inhibit angiogenesis and treat CNV, reaching the therapeutic responses comparable to that achieved by intravitreal injection of Eylea. Notably, the dosage of Eylea in FCS-based eyedrop formulation (1.4 mg per eye) was only 2.8 times of that used for intravitreal injection of free Eylea (0.5 mg per eye). Considering the greatly reduced industrial manufacture cost of recombinant antibodies in recent years, such an increase in antibody usage should be quite reasonable with tremendous market potential.

DISCUSSION

In this work, we developed a special ocular barrier penetrating polymer by modifying natural CS with fluorocarbon chains for macromolecular ophthalmic drug delivery to treat fundus diseases in eyedrop formulations. Such FCS could self-assemble with antibodies to form stable nanocomplexes and effectively deliver them into the retina and choroid by penetrating the ocular structural barriers without causing notable vision loss or other side effects to the treated animals. Mechanistic studies illustrated that FCS could induce the rearrangement of tight junction-associated proteins by promoting the phosphorylation of myosin light chain 2, leading to transitory opening of tight junctions between epithelial cells of corneal and conjunctival tissues and enabling intraocular penetration of FCS/protein complexes. In addition, the nonhydrophilic and nonlipophilic nature of fluorocarbon chains in FCS would likely make such nanocomplexes less "sticky," further promoting their intraocular penetration via both corneal-retinal and conjunctival-retinal pathways.

Afterward, we verified the therapeutic results in both a choroidal melanoma-bearing mouse model with FCS/anti-PDL1 eyedrops and CNV-bearing mouse and rabbit models with FCS/anti-VEGF antibody eyedrops. For choroidal melanoma treatment, FCS/anti-

PDL1 eyedrops could effectively inhibit tumor growth in the choroid by activating T cell immunity, reaching a therapeutic response superior to that achieved by intravenous injection of anti-PDL1 at the same antibody dose. For CNV treatment, FCS/anti-VEGFA eyedrops could markedly suppress CNV in mice by blocking VEGF expression, achieving therapeutic responses comparable to those observed after intravitreal injection of anti-VEGFA. FCS/Eylea eyedrops also achieved excellent therapeutic results in a CNV-bearing rabbit model, which is a closer model to human eyes in size scale and barrier structure. The antibody dosages needed for the eyedrop formulations were only 2.8-fold of that by intravitreal injection, indicating that our eyedrop formulation of antibodies exhibited extremely high potential for clinical transformation.

In summary, the ocular barrier penetration carrier FCS developed in our work may revolutionize the current strategy of fundus disease treatment, which usually requires intravitreal injections of therapeutic proteins (e.g., anti-VEGF for wet-AMD treatment). The eyedrop formulations of antibodies realized here would undoubtedly be superior to the intravitreal injection formulations in terms of patient compliance and side effect risks. Although further rigorous preclinical investigations are still required, the current pilot studies, especially those on rabbits with eyes on the same size scale as human eyes, demonstrated that our FCS-based eyedrop formulations of therapeutic proteins would have great possibility for future clinical translation in eye disease treatment. In future use for the patients, the antibiotic erythromycin may be added to prevent the potential risk of infection during the treatment. Our strategy may become a platform technology with tremendous market potential in the area of macromolecular ophthalmic drugs.

MATERIALS AND METHODS

Materials

CS (molecular weight = 340 kDa, degree of deacetylation percent (DD%) $\geq 95\%$) was purchased from Aladdin Industrial Co. (Shanghai, China). PFCA was purchased from Fluorochem Limited Co. *N*-(3-dimethylaminopropyl)-*N*-ethylcarbodiimide hydrochloride crystalline (EDC) and *N*-hydroxysuccinimide (NHS) were provided by JK Chemical Co. (Beijing, China). Dimethyl sulfoxide (DMSO) was purchased from Sangon Biotech Co. (Shanghai, China). PBS was obtained from Beijing Solarbio Science Technology Co. Dulbecco's modified Eagle's medium (DMEM)/Ham's F-12 medium, FBS, and penicillin/streptomycin were purchased from Life Technologies Co. (New York, USA). Anti-PDL1 (catalog no. BE0101) used for therapy was purchased from BIOCELL Biotech Co. Anti-VEGFA (catalog no. HPAB0330CQ), a kind of mouse anti-VEGFA recombinant antibody, used for therapy was purchased from Creative Biolabs Co. Eylea (catalog no. MB2806) used for therapy was purchased from Meilunbio Co. Rat IgG, FITC, and Cy5.5 were purchased from Sigma-Aldrich. The calcein-AM/PI double stain kit, bicinchoninic acid (BCA) protein assay kit, and CCK-8 cell viability kit were purchased from Beijing Solarbio Science Technology Co. The rat IgG ELISA kit was purchased from Thermo Fisher Scientific.

Cell lines

Human retinal pigment epithelial cells (human ARPE-19 cells), HCECs, and human umbilical vein endothelial cells (HUVECs)

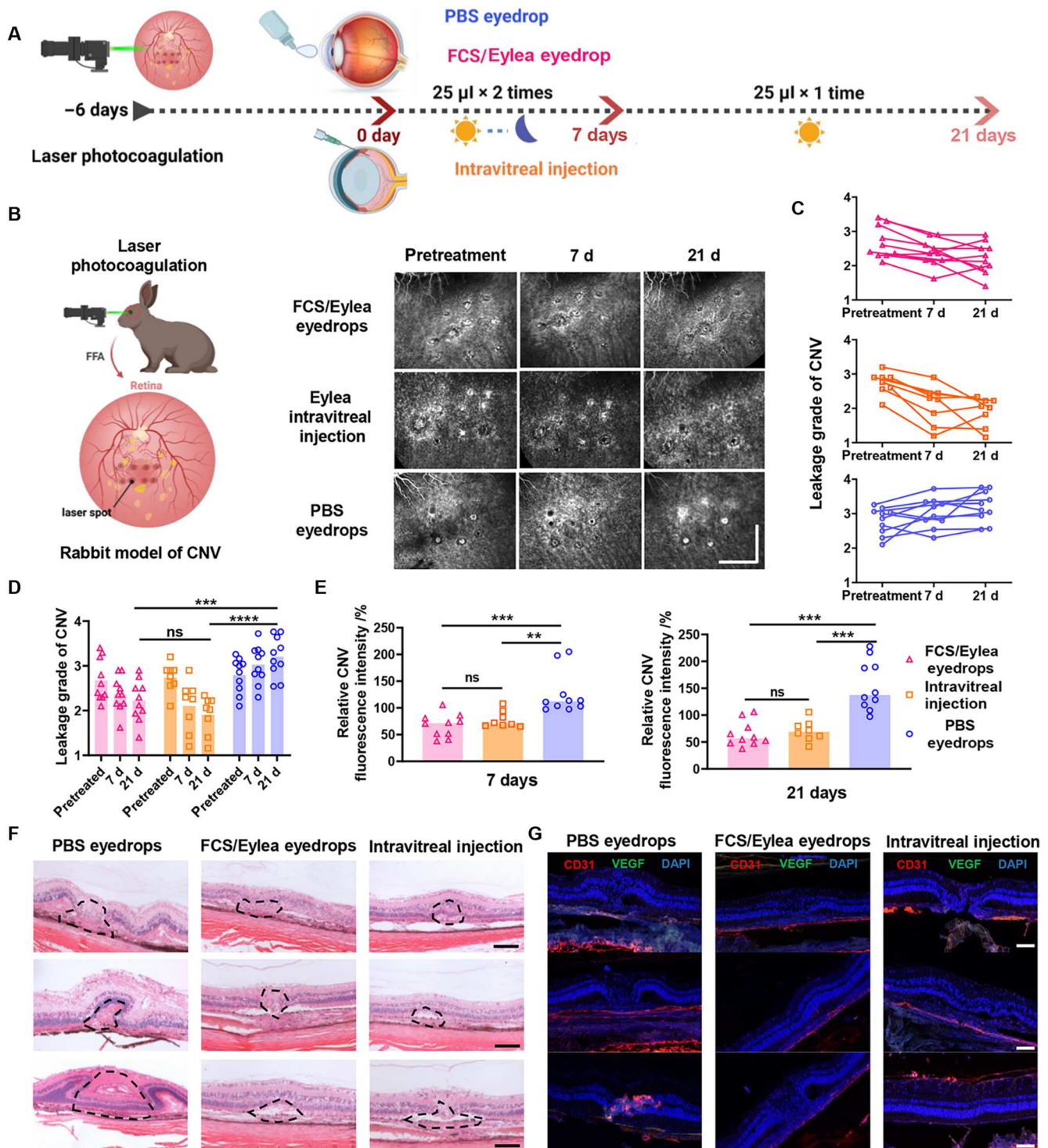


Fig. 7. FCS/Eylea eyedrops for CNV treatment in rabbits. (A) Schematic illustration of the establishment of NV-AMD in rabbits and the design of animal experiments. The experimental groups included (i) PBS eyedrops, (ii) FCS/Eylea eyedrops, and (iii) intravitreal injection of Eylea. (B) Representative FFA images of individual lesions in CNV-bearing rabbits during treatment on days 0, 15, and 30. Each laser point was indicated in a square (scale bar, 2 mm). (C) Expert grades of leakage in CNV by experienced pathologists in a double-blinded manner in different groups. (D) Statistical analysis of relative fluorescence intensities that present the leakage of angiogenic vessels in each laser point in CNV rabbits with different treatments on days 15 and 30 by ImageJ. (E) Representative H&E staining images of normal and individual lesions in the retina of CNV-bearing rabbits with different treatments (scale bars, 50 μ m). (F) Representative immunofluorescence images indicating the expression of VEGF and vascular distribution in individual lesions of CNV-bearing rabbits with different treatments (scale bars, 50 μ m). (G) Immunofluorescence staining images of CD31 and VEGF in the retinas of CNV-bearing rabbits with different treatments (scale bars, 50 μ m). Data were represented as means \pm SD. P values in (D) and (E) were calculated by using one-way ANOVA (** $P < 0.01$, *** $P < 0.001$, and **** $P < 0.0001$).

were obtained from the American Type Culture Collection (ATCC; Manassas, VA, USA) and validated using short tandem repeat analysis by Shanghai Biowing Applied Biotechnology Co. Ltd. HCECs, ARPE-19 cells, and HUVECs were cultured in DMEM containing 1% penicillin/streptomycin and 10% FBS at 37°C in 5% CO₂. The murine B16F10 melanoma cell line was purchased from ATCC and cultured in DMEM with high glucose containing 10% FBS and 1% penicillin sulfate and streptomycin at 37°C in 5% CO₂.

Animals

Female C57BL/6 mice, New Zealand rabbits, and purple blue rabbits were purchased from Nanjing Pengsheng Biological Technology Co. All animal experiments were performed in compliance with the relevant laws and approved by the Institutional Animal Care and Use Committee of Soochow University (no. ECSU-2019000198). The mice in operation were anesthetized through intraperitoneal injection with ketamine (100 mg/kg) and xylazine (10 mg/kg), and the rabbits were anesthetized through intramuscular injection with ketamine (40 mg/kg) and xylazine (5 mg/kg).

Synthesis of FCS

Perfluoroheptanoic acid was dissolved in DMSO and then mixed with EDC and NHS under stirring for 0.5 hours in the dark at room temperature to obtain activated perfluoroheptanoic acid (the molar ratio of perfluoroheptanoic acid, EDC, and NHS was 1:2:1). CS was dissolved in 1% acetic acid. Then, the activated perfluoroheptanoic acid was dropwise added to the CS solution under stirring in the dark for 20 hours. After stirring, 1 M HCl was directly added to the reaction system and stirred for another 0.5 hours. Last, excess anhydrous ethanol was added to precipitate the FCS-HCl product. Then, the product was washed and vacuum-dried. To obtain a series of FCS with different degrees of fluorocarbon substitutions, the feeding ratios between CS and PFCA were adjusted from 100:0 to 100:35 (Fig. 2B). The degree of substitution of conjugated fluoroalkyl substituents was characterized by ninhydrin colorimetry following the standard procedure (49). In addition, fluorine element analysis was used to calculate the degree of fluorination. Moreover, the molecular weight (measured by gel permeation chromatography), nuclear magnetic resonance, and Fourier infrared spectroscopy of the FCS were provided (fig. S29).

Preparation of FCS (or CS)/IgG nanocomplex

To prepare FCS (or CS)/IgG nanocomplexes, the synthesized FCS was mixed with rat IgG in PBS at different weight ratios (1: 4 to 4: 1) and stirred for 0.5 hours. The size, zeta potential, and dispersibility index of the obtained nanocomplex were measured with Zetasizer Nano ZS (Malvern Instrument), and the drug loading and drug encapsulation efficiency of FCS (or CS)/IgG nanocomplexes were measured by supercentrifuge (table S2). TEM (FEI TECNAI G2) was applied to observe the morphology of the representative nanocomplex. Moreover, FCS/anti-PDL1 and FCS/anti-VEGFA nanocomplexes were also prepared in the same way. Moreover, the secondary structure of antibodies in the nanocomplex was determined by circular dichroism spectroscopy (BRIGHTTIME), and the binding affinity of the antibody was determined by competitive ELISA according to a previous report (50).

Cumulative permeability of IgG using Franz diffusion

The fresh corneas of New Zealand rabbits were dissected and placed between the donor and receptor chambers of Franz diffusion (Fig. 2D and fig. S2). After verifying no leakage in the diffusion cell, each Franz diffusion cell was placed on a thermostatic stirrer (RYJ, China). Different samples were then added into the donor chamber (1-ml sample solution in donor chamber), and PBS was added into the receptor chamber (7-ml receptor solution in receptor chamber). A 0.3-ml receptor solution was collected, and 0.3-ml fresh receptor solution was replenished at 0-, 1-, 3-, and 6-hour time points. The concentration of penetrated IgG labeled with FITC was measured according to the fluorescence signal. The following formula was used to calculate the cumulative permeability

$$\text{Cumulative permeability} = [R_n \times V_1 + (R_{n-1} + R_{n-2} + R_{n-3} \dots + R_1) \times V_2] \times 100\% / R_{\text{all}} \times V_3$$

where R_n is the fluorescence value of the receptor solution at n th time collected, R_{n-1} is the fluorescence value of the receptor solution collected at the $n - 1$ th time, R_1 is the fluorescence value of the receptor solution collected at 1th time, R_{all} is the fluorescence value of the sample in the donor chamber, V_1 is the volume of the total receptor solution (the receptor chamber capacity is 7 ml), V_2 is the volume of collected solution (the collected solution is 0.3 ml every time), and V_3 is the volume of sample solution in the donor chamber (the total sample solution was 1 ml).

The penetration of IgG in different formulations after topical ophthalmic delivery

To measure the penetration of IgG in mouse eyes, eyedrops composed of FCS/IgG nanocomplexes (FCS, 2 mg/ml; IgG, 2 mg/ml, 5 μ l) or free IgG (IgG, 2 mg/ml, 5 μ l) were dropped in the eyes of anesthetized mice. Then, the mice were euthanized, and their eyes were harvested at different time points to measure the concentrations of rat IgG by ELISA kits.

To measure the penetration of IgG in mouse eyes, ¹²⁵I was labeled into the rat IgG, and eyedrops composed of FCS/¹²⁵I-IgG nanocomplexes (FCS, 2 mg/ml; ¹²⁵I-IgG, 2 mg/ml, 5 μ l) or free ¹²⁵I-IgG (¹²⁵I-IgG, 2 mg/ml, 5 μ l) were dropped in the right eye of anesthetized mice for 3 or 6 hours. Then, the mice were euthanized, and their eyes were harvested at different time points to measure the γ -ray intensity of rat ¹²⁵I-IgG in the eyeball after washing the ocular surface by PBS, and the penetration of ¹²⁵I-IgG was calculated by contrast with the γ -ray intensity of 5- μ l ¹²⁵I-IgG (¹²⁵I-IgG, 2 mg/ml).

To determine the penetration of IgG in rabbit eyes, eyedrops containing FCS/IgG nanocomplexes (FCS, 2 mg/ml; IgG, 2 mg/ml, 25 μ l) or free IgG (IgG, 2 mg/ml, 25 μ l) were dropped in eyes of anesthetized rabbits. Then, the rabbits in different groups were sacrificed, and their eyes were collected at different time points. The eyes were washed and dissected into the cornea, aqueous humor, iris, lens, vitreum, and retina, each part was weighed and lysed, and the concentration of IgG was measured using ELISA kits.

Immunocytochemistry analysis of tight junction proteins in HCECs

HCECs were cultured to form a corneal epithelial layer and then cocultured with FCS or CS at 100 μ g/ml according to cell safety test (figs. S30 and S31). One hour later, the cells were washed with PBS, fixed in 4% paraformaldehyde at 4°C for 20 min, permeabilized with 0.5% Triton X-100 at room temperature for 20 min,

blocked with 2% bovine serum albumin (BSA; in PBS) at room temperature for 1 hour, and then incubated with the following primary antibodies: anti-E-cadherin (1:500, Abcam, USA), anti-occludin (1:100, Abcam, USA), and anti-ZO-1 (1:100, Abcam, USA) at 4°C overnight. After washing away unbound primary antibodies, the cells were further incubated with FITC-conjugated secondary antibody (1:1000, Abcam, USA) at room temperature for 1 hour and then imaged by confocal laser scanning microscope (CLSM).

Western blotting analysis of tight junction proteins in HCECs

HCECs were cultured to form a corneal epithelial layer and then treated with FCS or CS at 100 µg/ml for 12 hours. Then, HCECs were lysed by IOP lysates (Beyotime, China) containing 0.1% protease inhibitor (Sigma-Aldrich, P8340) and 0.1% phosphatase inhibitor (Sigma-Aldrich, P2850) at 4°C for 30 min. Then, the cells were collected and centrifuged to obtain the supernatant, and the concentration of protein was measured by a BCA protein assay kit. Samples were diluted in protein loading buffer (Adipogen, USA), and 40 µg of protein was separated by SDS-polyacrylamide gel electrophoresis (Yamei, China) and transferred to a polyvinylidene difluoride membrane (Bio-Rad, China). The membranes were blocked with 5% BSA for 1 hour at room temperature and then incubated with primary antibodies, including anti-ZO-1 (1:500, Abcam, USA), anti-E-cadherin (1:10,000, Abcam, USA), anti-occludin (1:1000, Abcam, USA), anti-MLC (1:2000, Abcam, USA), anti-pMLC (1:2000, Abcam, USA), and anti-GAPDH (glyceraldehyde-3-phosphate dehydrogenase) (1:1000, Sangon Biotech, China), overnight at 4°C. After washing with tris-buffered saline (TBS)-Tween 20 (TBST) three times, the membranes were incubated with horseradish peroxidase-conjugated secondary antibodies (Abcam, USA) (1:5000 dilution) for 1 hour at room temperature. Last, the membranes were washed with TBST three times, incubated with ECL reagent (BBI Life Sciences Corporation, China), and imaged by the Amersham Imager 600 System (General Electric Company, USA).

TEER measurement assay

In this study, HCECs were seeded in Transwell insert chambers at a density of 5×10^4 cells per well, and the resistivity (R) of the cell layer was measured by R/V Meter of Epithelium (RE1600; Beijing KingTech Technology Co. Ltd.) every 2 days. Then, the TEER value was calculated according to the standard calculation method. While the TEER value of HCECs was stable, FCS or CS (FCS or CS, 100 µg/ml) was added to the insert chamber for 1 hour, and the TEER value was monitored at 1, 3, 6, and 12 hours. What is more, we added experiments in which the nanocomplexes were incubated with cells for 6 hours, and the TEER value was monitored at 6, 12, 24, 48, and 72 hours.

The following formula was used to calculate TEER ($\text{ohm}\cdot\text{cm}^2$)

$\text{TEER} (\text{ohm}\cdot\text{cm}^2) = (R_1 - R_0) \times 0.33$ where R_1 is the TEER value of inserts with cells and R_0 is the TEER value of inserts without cells. The insert membrane area in the plate was 0.33 cm^2 .

MLC phosphorylation inhibition

In this experiment, HCECs were seeded in the insert chamber of a Transwell at a density of 5×10^4 cells per well to form a barrier layer, and B16F10 cells, as the receptor, were seeded at a density of 2×10^5 cells per well in the lower chamber containing IFN- γ (0.05 µg/ml) to

stimulate B16F10 cells to overexpress PDL1. HCECs were pretreated with an ML-7 inhibitor (myosin light chain kinase inhibitor, $K_i = 300 \text{ nM}$) overnight. Then, the FCS/anti-PDL1 nanocomplex, CS/anti-PDL1 nanocomplex, or free anti-PDL1 (FCS or CS, 100 µg/ml; anti-PDL1, 100 µg/ml; $n = 3$) was added to HCEC layers and incubated for 6 hours. Then, B16F10 cells were collected, and the penetrated anti-PDL1 bound to PDL1 expressed on B16F10 cells was detected using a competitive method by flow cytometry (aPDL1-PE, BioLegend, catalog no. 124308).

Biocompatibility of FCS in mice

C57BL/6 mice were randomly divided into four groups (six eyeballs for each group) and treated with different eyedrops, including PBS, FCS (dissolved in PBS buffer), CS (dissolved in acetate-acetic acid buffer), and SDS (2 mg/ml, 5 µl each eye), twice every day for 4 weeks. Then, OCT (Heidelberg, Germany), an Espion E3 machine (Diagnosys, Boxborough, MA), a slit lamp, and a tonometer were used to monitor the changes in corneal thickness, retinal thickness, ERG, and IOP. Last, the eyes and main organs were collected for immunofluorescence staining and histological examination, and eyes were collected for cytokine detection using the TGF- β 1 Mouse ELISA Kit (Thermo Fisher Scientific, catalog no. BMS608-4), TNF- α Mouse ELISA Kit (Thermo Fisher Scientific, catalog no. BMS607-3), IL-1 β Mouse ELISA Kit (Thermo Fisher Scientific, catalog no. BMS6002), IL-6 Mouse ELISA Kit (Thermo Fisher Scientific, catalog no. BMS603-2), and IL-4 Mouse ELISA Kit (Thermo Fisher Scientific, catalog no. BMS613) and the blood was collected for routine blood biochemistry and blood analysis.

TUNEL assay

TUNEL (Sangon Biotech, China) was used to analyze cell death in the cornea after different treatments. Briefly, frozen slices of eye tissues were fixed with eyeball fixation solution for 15 min, washed with PBS three times, permeabilized in freshly prepared 0.1% Triton X-100, and then incubated with terminal deoxynucleotidyl transferase solution for 60 min at 37°C. Last, the samples were imaged by CLSM.

H&E staining

Eyeballs and other main organs, including the heart, liver, spleen, lung, and kidney of mice, together with the cornea and conjunctiva of rabbits, were collected and fixed in 4% paraformaldehyde solution, embedded in paraffin, and cut into sections (5 µm thick). Then, the tissue sections were stained with H&E and imaged by light microscopy (DM 4000).

In vivo treatment of choroidal melanoma

To evaluate the therapeutic effect, a choroidal melanoma mouse model was established by injecting 2×10^5 luciferase B16F10 cells in 5 µl of PBS between the retina and choroid in the right eye of each mouse. Two days later, mice were randomly divided into five groups ($n = 8$): (i) PBS eyedrops (5 µl per day \times 8 days), (ii) intravenous administration of anti-PDL1 (anti-PDL1, 4 mg/kg, 1 mg/kg for each time), (iii) free anti-PDL1 eyedrops (anti-PDL1, 4 mg/kg, 5 µl per day \times 8 days), (iv) FCS eyedrops (4 mg/kg, 5 µl per day \times 8 days), and (v) FCS/anti-PDL1 nanocomplex eyedrops (anti-PDL1, 4 mg/kg; FCS, 4 mg/kg, 5 µl per day \times 8 days). To evaluate the therapeutic results, mice were intraperitoneally injected with D-luciferin

potassium salt (10 mg/kg) and imaged by the in vivo imaging instrument (IVIS) spectrum system with a 60-s exposure time.

Analysis of different immune cells

To study the immune cells in choroidal melanoma tumors after different treatments, the mice were sacrificed, and their eyes were collected and cut into small pieces to obtain single-cell suspensions 12 days after different treatments. Then, the cells were dispersed in PBS (pH 7.4) containing 1% heat-inactivated FBS to stain with different antibodies. First, the anti-CD16/32 antibodies (BioLegend, catalog no. 101302) were added to the cells to block the Fc receptors. Then, the cells were stained with fluorescence-labeled antibodies, including anti-CD3-FITC (BioLegend, catalog no. 100204), anti-CD4-APC (allophycocyanin) (BioLegend, catalog no. 100412), anti-CD8-PE (phycoerythrin) (BioLegend, catalog no. 100708), and anti-GranzB-PerCP (peridinin chlorophyll protein) (BioLegend, catalog no. 149704). In the parallel experiment, the supernatant of cells was collected to measure the concentration of IFN- γ by ELISA Kit (Thermo Fisher Scientific, catalog no. 88-7314-88) according to the manufacturer's instructions.

In vivo treatment of CNV in mice

To evaluate the therapeutic results of CNV using different anti-VEGFA formulations, we first built a mouse CNV model by performing three to five laser photocoagulations (532 nm, 475 mW, 0.05 s, and 50 μ m) on the right eye around the optic nerve of each mouse according to the standard protocol (48, 51). To image the formation of CNV lesions in eyes, mice were intraperitoneally injected with 0.1 ml of 2% fluorescein sodium (Alcon) and then imaged by an SD-OCT system (Heidelberg, Germany). Seven days later, the mice were randomly divided into five groups: (i) PBS eye-drops (5 μ l per day \times 14 days, $n = 6$), (ii) anti-VEGFA eyedrops (the total dose of anti-VEGFA was 14 mg/kg, 5 μ l per day \times 14 days, $n = 6$), (iii) FCS eyedrops (the total dose of anti-VEGFA was 14 mg/kg, 5 μ l per day \times 14 days, $n = 6$), (iv) FCS/anti-VEGFA nanocomplex eyedrops (the total dose of anti-VEGFA was 14 mg/kg; FCS, 14 mg/kg, 5 μ l per day \times 14 days, $n = 6$), and (v) intravitreal injections of anti-VEGFA (the total dose of anti-VEGFA was 2.5 mg/kg, 5 μ l one-time injection, $n = 6$). The original structure and binding affinity of anti-VEGFA remained nearly unchanged owing to the noncovalent interaction between FCS and antibodies (fig. S32). To measure the therapeutic results, the spindle-shaped hyper-reflective area [the direction of the long axis was consistent with the level of the retinal pigment epithelium (RPE)] was calculated according to the thickness of the CNV lesion by ImageJ, and the leakage of CNV was assessed according to the vascular leakage area and quantitated according to the intensity of sodium fluorescein by ImageJ (52). To evaluate the area of each CNV, we calculated the area of laser spots of the entire optic disc rather than a single laser spot. As shown in fig. S21, we evaluated the area of selected laser burns that was labeled by dotted lines. Moreover, ERG was performed at the end of treatment to examine the optic function of the mice. Twenty-two days after different treatments, the CNV-bearing eyes of mice in different groups were collected for histological examination and immunofluorescence staining of RPE65, VEGF, and IL-1 β .

In vivo treatment of CNV in rabbits

The purple blue rabbit CNV model was built by performing nine laser photocoagulations (659 nm, 300 mW, 0.05 s, and 50 μ m) on the right eyes under the optic nerve of each rabbit. Six days later, the rabbits were randomly divided into three groups: (i) PBS eyedrops (25 μ l per day \times 21 days, $n = 10$), (ii) FCS/Eylea nanocomplex eyedrops (Eylea, 1.4 mg per eye; 2 mg/ml for 25 μ l twice a day for the first 7 days and then 25 μ l per day for the next 14 days, $n = 10$), and (iii) intravitreal injection of Eylea (Eylea, 0.5 mg per eye; 10 mg/ml for 50 μ l one-time injection, $n = 8$). The total Eylea dose of FCS/Eylea eyedrops was 1.4 mg per eye, and the total Eylea dose of intravitreal injection was 0.5 mg per eye, which is according to clinical Eylea treatment's dose. To image the formation of CNV lesions in rabbit eyes and evaluate the therapeutic results, 0.15 ml of 10% sodium fluorescein was injected into the vein of the rabbit ear, and then, sequential real-time FFA images were captured and quantitated according to the intensity of sodium fluorescein by ImageJ. The leakage grades of CNV were independently assessed by five specialists according to the following grading criteria of FFA images: grade I indicates no hyperfluorescence, grade II indicates hyperfluorescence without leakage, grade III indicates hyperfluorescence with leakage, and grade IV indicates bright hyperfluorescence with increased intensity and size and severe leakage. Moreover, 30 days after different treatments, the CNV-bearing rabbits in different groups were sacrificed, and their eyes were collected for histological examination and immunofluorescence staining of VEGF and CD31.

Statistical analysis

All statistical analyses were evaluated by GraphPad Prism (PRISM 8.3.0; GraphPad Software, 2019). All data are presented as the mean \pm SEM. Two-tailed Student's t test was used for two-group comparisons, and one-way analysis of variance (ANOVA) with a Tukey post hoc test was used for multiple comparisons. The threshold for statistical significance was $*P < 0.05$, $**P < 0.01$, $***P < 0.001$, and $****P < 0.0001$. All figure illustrations were created with BioRender.com.

Supplementary Materials

This PDF file includes:

Figs. S1 to S32
Tables S1 and S2

Other Supplementary Material for this manuscript includes the following:

Movie S1

[View/request a protocol for this paper from Bio-protocol.](#)

REFERENCES AND NOTES

1. M. C. Ibanez-Bruron, A. L. Solebo, P. M. Cumberland, J. S. Rahi, Methods of ascertainment of children and young people living with diabetes mellitus: A mapping exercise of National Health Service diabetic eye screening programmes. *Lancet* **388**, 559 (2016).
2. World Health Organization, *World Report on Vision* (World Health Organization, 2019).
3. L. D. Chong, Barrier maintenance. *Science* **338**, –1512 (2012).
4. Z. Wang, C.-H. Liu, S. Huang, Z. Fu, Y. Tomita, W. R. Britton, Wnt signaling activates MFSD2A to suppress vascular endothelial transcytosis and maintain blood-retinal barrier. *Sci. Adv.* **6**, eaba7457 (2020).
5. J. S. Heier, S. Kherani, S. Desai, P. Dugel, S. Kaushal, S. H. Cheng, C. Delacono, A. Purvis, S. Richards, A. L. Halpern, J. Connelly, S. C. Wadsworth, R. Varona, R. Buggage, A. Scaria,

- P. A. Campochiaro, Intravitreal injection of AAV2-sFLT01 in patients with advanced neovascular age-related macular degeneration: A phase 1, open-label trial. *Lancet* **390**, 50–61 (2017).
6. G. B. Melo, N. F. S. da Cruz, G. G. Emerson, F. A. Rezende, C. H. Meyer, S. Uchiyama, J. Carpenter, H. F. Shiroma, M. E. Farah, M. Maia, E. B. Rodrigues, Critical analysis of techniques and materials used in devices, syringes, and needles used for intravitreal injections. *Prog. Retin. Eye Res.* **80**, 100862 (2021).
 7. C. R. Bauml, R. F. Spaide, L. Vajzovic, K. B. Freund, S. D. Walter, V. John, R. Rich, N. Chaudhry, R. R. Lakhanpal, P. R. Oellers, T. K. Leveque, B. K. Rutledge, M. Chittum, T. Bacci, A. B. Enriquez, N. J. Sund, E. N. P. Subong, T. A. Albin, Retinal vasculitis and intraocular inflammation after intravitreal injection of brolicizumab. *Ophthalmology* **127**, 1345–1359 (2020).
 8. J. B. Jonas, R. F. Degenring, I. Kreissig, I. Akkoyun, B. A. Kampeter, Intraocular pressure elevation after intravitreal triamcinolone acetonide injection. *Ophthalmology* **112**, 593–598 (2005).
 9. J. J. Chae, J. H. Jung, W. Zhu, B. G. Gerberich, M. R. B. Fard, H. E. Grossniklaus, C. R. Ethier, M. R. Prausnitz, Drug-free, nonsurgical reduction of intraocular pressure for four months after suprachoroidal injection of hyaluronic acid hydrogel. *Adv. Sci.* **8**, 2001908 (2021).
 10. Y. C. Kim, M. D. Shin, S. F. Hackett, H. T. Hsueh, R. L. Silva, A. Date, H. Han, B.-J. Kim, A. Xiao, Y. Kim, L. Ogunnaike, N. M. Anders, A. Hemingway, P. He, A. S. Jun, P. J. McDonnell, C. Eberhart, I. Pitha, D. J. Zack, P. A. Campochiaro, J. Hanes, Gelling hypotonic polymer solution for extended topical drug delivery to the eye. *Nat. Biomed. Eng.* **4**, 1053–1062 (2020).
 11. S. H. Park, D. H. Job, C. S. Chob, K. Leea, J. H. Kimb, S. Ryua, C. Jooa, J. H. Kim, W. Ryua, Depthwise-controlled scleral insertion of microneedles for drug delivery to the back of the eye. *Eur. J. Pharm. Biopharm.* **133**, 31–41 (2018).
 12. A. Abramson, E. Caffarel-Salvador, V. Soares, D. Minahan, R. Y. Tian, X. Lu, D. Dellal, Y. Gao, S. Kim, J. Wainer, J. Collins, S. Tamang, A. Hayward, T. Yoshitake, H.-C. Lee, J. Fujimoto, J. Fels, M. R. Frederiksen, U. Rahbek, N. Roxhed, R. Langer, G. Traverso, A luminal unfolding microneedle injector for oral delivery of macromolecules. *Nat. Med.* **25**, 1512–1518 (2019).
 13. A. Than, C. Liu, H. Chang, P. K. Duong, C. M. G. Cheung, C. Xu, X. Wang, P. Chen, Self-implantable double-layered micro-drug-reservoirs for efficient and controlled ocular drug delivery. *Nat. Commun.* **9**, 4433 (2018).
 14. X. Zhao, I. Seah, K. Xue, W. Wong, Q. S. W. Tan, X. Ma, Q. Lin, J. Y. C. Lim, Z. Liu, B. H. Parikh, K. N. Mehta, J. W. Lai, B. Yang, K. C. Tran, V. A. Barathi, K. H. Cheong, W. Hunziker, X. Su, X. J. Loh, Antiangiogenic nanomicelles for the topical delivery of aflibercept to treat retinal neovascular disease. *Adv. Mater.* **34**, 2108360 (2021).
 15. A. Lepetier, J. Madore, J. S. O'Donnell, R. L. Johnston, X.-Y. Li, E. McDonald, E. Ahern, A. Kuchel, M. Eastgate, S.-A. Pearson, D. Mallardo, P. A. Ascierto, D. Massi, B. Merelli, M. Mandala, J. S. Wilmott, A. M. Menzies, C. Leduc, J. Stagg, B. Routy, G. V. Long, R. A. Scolyer, T. Bald, N. Waddell, W. C. Dougall, M. W. L. Teng, M. J. Smyth, Tumor CD155 expression is associated with resistance to anti-PD1 immunotherapy in metastatic melanoma. *Clin. Cancer Res.* **26**, 3671–3681 (2020).
 16. H. Mehta, A. Tufail, V. Daien, A. Y. Lee, V. Nguyen, M. Ozturk, D. Barthelmes, M. C. Gillies, Real-world outcomes in patients with neovascular age-related macular degeneration treated with intravitreal vascular endothelial growth factor inhibitors. *Prog. Retin. Eye Res.* **65**, 127–146 (2018).
 17. D. Thacharodi, K. P. Rao, Development and *in vitro* evaluation of chitosan-based transdermal drug delivery systems for the controlled delivery of propranolol hydrochloride. *Biomaterials* **16**, 145–148 (1995).
 18. T.-H. Yeh, L.-W. Hsu, M. T. Tseung, P.-L. Lee, K. Sonjae, Y.-C. Ho, H.-W. Sung, Mechanism and consequence of chitosan-mediated reversible epithelial tight junction opening. *Biomaterials* **32**, 6164–6173 (2011).
 19. K. Sonaje, K.-J. Lin, J.-J. Wang, F.-L. Mi, C.-T. Chen, J.-H. Juang, H.-W. Sung, Self-assembled pH-sensitive nanoparticles: A platform for oral delivery of protein drugs. *Adv. Funct. Mater.* **20**, 3695–3700 (2010).
 20. P. Mukhopadhyay, R. Mishra, D. Rana, P. P. Kundu, Strategies for effective oral insulin delivery with modified chitosan nanoparticles: A review. *Prog. Polym. Sci.* **37**, 1457–1475 (2012).
 21. I. Woichansky, C. A. Beretta, N. Berns, V. Riechmann, Three mechanisms control E-cadherin localization to the zonula adherens. *Nat. Commun.* **7**, 10834 (2016).
 22. G. Rinaldo, I. Marigliano, I. Vespignani, G. Perozzi, Y. Sambuy, The effect of chitosan and other polycations on tight junction permeability in the human intestinal Caco-2 cell line. *J. Nutr. Biochem.* **13**, 157–167 (2002).
 23. J. Hu, N. Gao, Y. Zhang, X. Chen, J. Li, F. Bian, W. Chi, Z. Liu, C. S. Paiva, S. C. Pflugfelder, D.-Q. Li, IL-33/ST2/IL-9/IL-9R signaling disrupts ocular surface barrier in allergic inflammation. *Mucosal Immunol.* **13**, 919–930 (2020).
 24. R. Fernandez-Godino, D. L. Garland, E. A. Pierce, Isolation, culture and characterization of primary mouse RPE cells. *Nat. Protoc.* **11**, 1206–1218 (2016).
 25. M.-L. Chen, F.-M. Tsai, M.-C. Lee, Y.-Y. Lin, Antipsychotic drugs induce cell cytoskeleton reorganization in glial and neuronal cells via Rho/Cdc42 signal pathway. *Prog. Neuro-psychopharmacol. Biol. Psychiatry* **71**, 14–26 (2016).
 26. S. Sayedyhossein, A. Rudkouskaya, V. Leclerc, L. Dagnino, Integrin-linked kinase is indispensable for keratinocyte differentiation and epidermal barrier function. *J. Invest. Dermatol.* **136**, 425–435 (2016).
 27. D. Daassi, K. M. Mahoney, G. J. Freeman, The importance of exosomal PD-L1 in tumour immune evasion. *Nat. Rev. Immunol.* **20**, 209–215 (2020).
 28. S. Ohkubo, N. Nakahata, Y. Ohizumi, ML-7 and W-7 facilitate thromboxane A₂-mediated Ca²⁺ mobilization in rabbit platelets. *Eur. J. Pharmacol.* **298**, 175–183 (1996).
 29. K.-P. Xu, X.-F. Li, F.-S. X. Yu, Corneal organ culture model for assessing epithelial responses to surfactants. *Toxicol. Sci.* **58**, 306–314 (2000).
 30. J. Wu, Z. Zhu, W. Liu, Y. Zhang, Y. Kang, J. Liu, C. Hu, R. Wang, M. Zhang, L. Chen, L. Shao, How nanoparticles open the paracellular route of biological barriers: Mechanisms, applications, and prospects. *ACS Nano* **16**, 15627–15652 (2022).
 31. R. Rosenthal, D. Günzel, C. Finger, S. M. Krug, J. F. Richter, J.-D. Schulzke, M. Fromm, S. Amasheh, The effect of chitosan on transcellular and paracellular mechanisms in the intestinal epithelial barrier. *Biomaterials* **33**, 2791–2800 (2012).
 32. M. J. Jager, C. L. Shields, C. M. Cebulla, M. H. Abdel-Rahman, H. E. Grossniklaus, M.-H. Stern, R. D. Carvajal, R. N. Belfort, R. Jia, J. A. Shields, B. E. Damato, Uveal melanoma. *Nat. Rev. Dis. Primers* **6**, 24 (2020).
 33. D. Reichstein, K. Karan, Endoresection utilizing pars plana vitrectomy for benign and malignant intraocular tumors. *Curr. Opin. Ophthalmol.* **30**, 151–158 (2019).
 34. S. K. Houston, C. C. Wykoff, A. M. Berrocal, D. J. Hess, T. G. Murray, Lasers for the treatment of intraocular tumors. *Lasers Med. Sci.* **28**, 1025–1034 (2013).
 35. A. Kalbasi, A. Ribas, Tumour-intrinsic resistance to immune checkpoint blockade. *Nat. Rev. Immunol.* **20**, 25–39 (2020).
 36. B. A. Helmink, P.-O. Gaudreau, J. A. Wargo, Immune checkpoint blockade across the cancer care continuum. *Immunity* **48**, 1077–1080 (2018).
 37. Z. Fehervari, Blood–brain barrier integrity. *Nat. Immunol.* **20**, 1 (2019).
 38. M. Chen, C. Luo, J. Zhao, G. Devarajan, H. Xu, Immune regulation in the aging retina. *Prog. Retin. Eye Res.* **69**, 159–172 (2019).
 39. J. Li, S. Yang, Y. Deng, P. Chai, Y. Yang, X. He, X. Xie, Z. Kang, G. Ding, H. Zhou, X. Fan, Emancipating target-functionalized carbon dots from autophagy vesicles for a novel visualized tumor therapy. *Adv. Funct. Mater.* **28**, 1800881 (2018).
 40. M. R. Middleton, C. McAlpine, V. K. Woodcock, P. Corrie, J. R. Infante, N. M. Steven, T. R. J. Evans, A. Anthoney, A. N. Shoushtari, O. Hamid, A. Gupta, A. Vardeu, E. Leach, R. Naidoo, S. Stanhope, S. Lewis, J. Hurst, I. O'Kelly, M. Szno, Tebentafusp, A TCR/anti-CD3 bispecific fusion protein targeting gp100, potentially activated antitumor immune responses in patients with metastatic melanoma. *Clin. Cancer Res.* **26**, 5869–5878 (2020).
 41. B. E. Damato, J. Dukes, H. Goodall, R. D. Carvajal, Tebentafusp: T cell redirection for the treatment of metastatic uveal melanoma. *Cancers (Basel)* **11**, 971 (2019).
 42. S. Abdulkadir, C. Li, W. Jiang, X. Zhao, P. Sang, L. Wei, Y. Hu, Q. Li, J. Cai, Modulating angiogenesis by proteomimetics of vascular endothelial growth factor. *J. Am. Chem. Soc.* **144**, 270–281 (2022).
 43. M. E. Pennesi, M. Neuringer, R. J. Courtney, Animal models of age related macular degeneration. *Mol. Aspects Med.* **33**, 487–509 (2012).
 44. S. Datta, M. Cano, K. Ebrahimi, L. Wang, J. T. Handa, The impact of oxidative stress and inflammation on RPE degeneration in non-neovascular AMD. *Prog. Retin. Eye Res.* **60**, 201–218 (2017).
 45. J. G. Hollyfield, V. L. Bonilha, M. E. Rayborn, X. Yang, K. G. Shadrach, L. Lu, R. L. Ufret, R. G. Salomon, V. L. Perez, Oxidative damage-induced inflammation initiates age-related macular degeneration. *Nat. Med.* **14**, 194–198 (2008).
 46. R. Natoli, N. Fernando, M. Madigan, J. A. Chu-Tan, K. V. J. Provis, M. Rutar, Microglia-derived IL-1 β promotes chemokine expression by Müller cells and RPE in focal retinal degeneration. *Mol. Neurodegener.* **12**, 31 (2017).
 47. Y. Son, D. Lim, S. Park, I.-K. Song, J.-H. Kim, S. Shin, H. Jang, K.-H. Liu, Y. O, G.-Y. Song, W. Kang, Y.-S. Cho, M. K. Na, H. Chung, S. Oh, Ilimaquinone inhibits neovascular age-related macular degeneration through modulation of Wnt/ β -catenin and p53 pathways. *Pharmacol. Res.* **161**, 105146 (2020).
 48. V. Lambert, J. Lecomte, S. Hansen, S. Blacher, M.-L. A. Gonzalez, I. Struman, N. E. Sounni, E. Rozet, P. Tullio, J. M. Foidart, J.-M. Rakic, A. Noel, Laser-induced choroidal neovascularization model to study age-related macular degeneration in mice. *Nat. Protoc.* **8**, 2197–2211 (2013).
 49. Z. Zhang, W. Shen, J. Ling, Y. Yan, J. Hu, Y. Cheng, The fluorination effect of fluoroamphiphiles in cytosolic protein delivery. *Nat. Commun.* **9**, 1377 (2018).
 50. M. Yi, J. Zhang, A. Li, M. Niu, Y. Yan, Y. Jiao, S. Luo, P. Zhou, K. Wu, The construction, expression, and enhanced anti-tumor activity of YM101: A bispecific antibody simultaneously targeting TGF- β and PD-L1. *J. Hematol. Oncol.* **14**, 27 (2021).

51. S. L. Doyle, M. Campbell, E. Ozaki, R. G. Salomon, A. Mori, P. F. Kenna, G. J. Farrar, A. Kiang, M. M. Humphries, E. C. Lavelle, L. A. J. O'Neill, J. G. Hollyfield, P. Humphries, NLRP3 has a protective role in age-related macular degeneration through the induction of IL-18 by drusen components. *Nat. Med.* **18**, 791–798 (2012).
52. M. Bolz, U. Schmidt-Erfurth, G. Deak, G. Mylonas, K. Kriechbaum, C. Scholda; Diabetic Retinopathy Research Group Vienna, Optical coherence tomographic hyperreflective Foci: A morphologic sign of lipid extravasation in diabetic macular edema. *Ophthalmology* **116**, 914–920 (2009).

Acknowledgments

Funding: This work was partially supported by the National Research Programs of China (2021YFF0701800 and 2020YFA0211100), the National Natural Science Foundation of China (52032008, 91959104, 21927803, 51903182, and 52250002), the Government of Jiangsu Province (BK20190826), Collaborative Innovation Center of Suzhou Nano Science and Technology, and Suzhou Key Laboratory of Nanotechnology and Biomedicine 111 Program from the Ministry of Education of China. **Author contributions:** Z.L., Q.C., and J.S. conceived the project and designed the studies. J.S., Z.L., Q.C., H.G., P.G., and Xiaofeng Zhang carried out and

analyzed anatomical, behavioral, and electrophysiological studies. J.S., Z.L., Q.C., L.C., T.W., Y.C., and N.L. designed, carried out, and analyzed material synthesis. J.S., Z.L., Q.C., Y.J., Y.W., M.C., and J.Z. designed, carried out, and analyzed in vitro experiments. J.S., H.G., S.L., Y.J., Y.L., Jipeng Li, Juan Liang, and Xiaoyu Zu contributed to carry out and analyzed in vivo treatment experiments. All authors discussed the results and commented on the manuscript. **Competing interests:** Z.L., Q.C., and J.S. have obtained an authorized patent (202010063620.5) from the State Intellectual Property Office (China). Z.L., Q.C., T.W., and J.S. have applied for patents (202010061971.2 and PCT/CN2020/138465) from the State Intellectual Property Office (China) as well as from the U.S. Patent Office (US17/630,143) and the European Patent Office (20915498.8). The authors declare no other competing interests. **Data and materials availability:** All data needed to evaluate the conclusions in the paper are present in the paper and/or the Supplementary Materials.

Submitted 31 March 2022

Accepted 27 December 2022

Published 27 January 2023

10.1126/sciadv.abq3104